

## REPORT DOCUMENTATION PAGE

Form Approved OMB No. 0704-0188

maintaining the data needed, and completing and reviewing the collection of information. Send comments regarding this burden estimate or any other aspect of this collection of information, including suggestions for reducing the burden, to Department of Defense, Washington Headquarters Services, Directorate for Information Operations and Reports (0704-0188), 1215 Jefferson Davis Highway, Suite 1204, Arlington, VA 22202-4302. Respondents should be aware that notwithstanding any other provision of law, no person shall be subject to any penalty for failing to comply with a collection of information if it does not display a currently valid OMB control number.

PLEASE DO NOT RETURN YOUR FORM TO THE ABOVE ADDRESS.

1. REPORT DATE (DD-MM-YYYY)			2. REPORT TYPE		3. DATES COVERED (From - To)
			Final Report		6 September 2002 - 06-Sep-03
4. TITLE AND SUBTITLE			5a. CONTRACT NUMBER FA8655-02-M4034		
Chemical Microrocket: Scaling and Performance Enhancement			5b. GRANT NUMBER		
			5c. PROGRAM ELEMENT NUMBER		
6. AUTHOR(S)			5d. PROJECT NUMBER		
Professor Claudio Bruno			5d. TASK NUMBER		
			5e. WORK UNIT NUMBER		
7. PERFORMING ORGANIZATION NAME(S) AND ADDRESS(ES)				8. PERFORMING ORGANIZATION REPORT NUMBER	
University of Rome Via Eudossiana 18 Rome 00184 Italy				N/A	
9. SPONSORING/MONITORING AGENCY NAME(S) AND ADDRESS(ES)				10. SPONSOR/MONITOR'S ACRONYM(S)	
EOARD PSC 802 BOX 14 FPO 09499-0014				11. SPONSOR/MONITOR'S REPORT NUMBER(S) SPC 02-4034	
12. DISTRIBUTION/AVAILABILITY STATEMENT					
Approved for public release; distribution is unlimited.					
13. SUPPLEMENTARY NOTES					
14. ABSTRACT					
This report results from a contract tasking University of Rome as follows: The ultimate objective of this work is to find criteria for designing high thrust (chemical) microrocket for mini- and microsatellites.					
15. SUBJECT TERMS					
EOARD, Combustion Modeling, micro scale flows, Catalysis					
16. SECURITY CLASSIFICATION OF:			17. LIMITATION OF ABSTRACT	18. NUMBER OF PAGES	19a. NAME OF RESPONSIBLE PERSON
a. REPORT UNCLAS	b. ABSTRACT UNCLAS	c. THIS PAGE UNCLAS	UL	53	Ingrid J. Wysong
19b. TELEPHONE NUMBER (Include area code) +44 (0)20 7514 4285					

# **Chemical MicroRocket: Scaling and Performance Enhancement**

## **—FINAL REPORT—**

**Claudio Bruno<sup>\*</sup>, Eugenio Giacomazzi<sup>†</sup>, Antonella Ingenito<sup>‡</sup>**

University of Rome “La Sapienza”  
Department of Mechanics and Aeronautics  
Via Eudossiana, 18  
00184 - ROME (ITALY)

<sup>\*</sup>E-Mail: [bruno@dma.ing.uniroma1.it](mailto:bruno@dma.ing.uniroma1.it) Tel.: +39.0644585.280 Fax: +39.064881759

<sup>†</sup>E-Mail: [eugenio@pcmerlino.ing.uniroma1.it](mailto:eugenio@pcmerlino.ing.uniroma1.it) Tel.: +39.0644585.272

<sup>‡</sup> E-Mail: [antonella@pcmerlino.ing.uniroma1.it](mailto:antonella@pcmerlino.ing.uniroma1.it) Tel.: +39.0644585.272

**THE CONTRACTOR, CLAUDIO BRUNO, HEREBY DECLARES THAT, TO THE BEST OF ITS KNOWLEDGE AND BELIEF, THE TECHNICAL DATA DELIVERED HEREWITH UNDER CONTRACT NO. FA8655-02-M034 (REFERENCE SPC 02-4034) IS COMPLETE, ACCURATE, AND COMPLIES WITH ALL REQUIREMENTS OF THE CONTRACT.**

**"I CERTIFY THAT THERE WERE NO SUBJECT INVENTIONS TO DECLARE AS DEFINED IN FAR 52.227-13, DURING THE PERFORMANCE OF THIS CONTRACT."**

**25TH JULY 2003**

**PROFESSOR CLAUDIO BRUNO**

---

## Contents

<b>I Scaling and Performance Enhancement</b>	<b>1</b>
1 Introduction	1
2 Scaling and Transport Equations	2
3 Scaling: Performance	3
3.1 Thrust Analysis . . . . .	4
3.2 Chamber Temperature Analysis and Effect of Reforming . . . . .	6
4 Scaling: Turbulent Mixing and Combustion	8
4.1 Quenching . . . . .	9
5 Scaling: Laminar Combustion	10
6 Conclusions	11
<b>II Methanol Cracking and Performance</b>	<b>13</b>
1 Introduction	13
2 Chemical Calculations	13
2.1 Cracking: Equilibrium Analysis . . . . .	14
3 Equilibrium Performance	17
4 Conclusions	29
<b>III Catalytic Combustion Enhancement</b>	<b>30</b>
1 Introduction	30
2 Catalysis and Reforming in MicroRockets	31
2.1 Scaling of the Catalytic Heat Release . . . . .	34
3 Effects on Thrust and Quenching	35
4 Conclusions	36

<b>IV Aluminum/Water Operation</b>	<b>38</b>
<b>1 Introduction</b>	<b>38</b>
<b>2 Aluminum/Water: Theoretical Performance</b>	<b>38</b>
<b>3 Burning aluminum particles with steam: Heating times</b>	<b>43</b>
<b>4 Kinetics and Ignition</b>	<b>47</b>
<b>5 Impact on flame anchoring</b>	<b>49</b>
<b>6 Preliminary conclusions</b>	<b>49</b>

## Nomenclature

### Symbols:

$A$ : area	$Pr$ : Prandtl number
$A_i$ : constant, $i = 1, \dots, 4$	$\dot{Q}$ : heat release
$CF$ : thrust coefficient	$R$ : gas constant
$C_p$ : specific heat at constant pressure	$\mathfrak{R}_u$ : universal gas constant
$C_l$ : liquid phase specific heat	$R_{al}$ : radius of aluminum particle
$C_s$ : solid phase specific heat	$Re$ : Reynolds number
$C_w$ : wall heat transfer coefficient	$S_L$ : laminar flame speed
$D$ : engine characteristic size	$T_b$ : boiling temperature
$D_{st}$ : diffusion coefficient at stoichiometric conditions	$T_g$ : rocket chamber temperature
$D_{12}$ : diffusion coefficient, binary mixture	$T_l$ : liquid phase temperature
$d$ : injector characteristic size	$T_m$ : melting temperature
$E_a$ : activation energy	$T_o$ : reference temperature
$F$ : thrust	$T_s$ : solid phase temperature
$h$ : heat transfer coefficient	$T_w$ : rocket chamber wall temperature
$I_{sp}$ : specific impulse	$T_i$ : propellant injectors temperature
$k$ : thermal conductivity	$t$ : time
$L$ : engine characteristic length	$t_{Al_2O_3}$ : thickness of alumina particle
$l$ : length	$t_{ch}$ : chemical time
$M_W$ : molecular weight	$U$ : average velocity in rocket chamber
$\dot{m}$ : mass flow rate	$V_e$ : nozzle exhaust velocity
$m = D/d$	$W_{TOT}$ : total chemical heat release
$n$ : order of chemical reaction	$W_{TRANS}$ : power transported to the walls
$Nu$ : Nusselt number	$W_{SP}$ : power/unit volume
$P_e$ : nozzle exit pressure	$x$ : coordinate
$P_o$ : rocket chamber pressure	$Y$ : mass fraction
	$Z$ : mixture fraction

### Greek Symbols:

$\Delta H_R$ : reaction heat	$\lambda$ : turbulent length scale
$\alpha_l$ : liquid phase thermal diffusivity	$\mu$ : molecular viscosity
$\alpha_s$ : solid phase thermal diffusivity	$\mu_o$ : molecular viscosity at $T_o$
$\varepsilon$ : turbulent dissipation	$\eta_\mu$ : viscous losses factor
$\gamma$ : specific heat ratio	$\rho$ : density
$\kappa$ : thermal conductivity	$\chi$ : strain rate

### Subscripts:

$12$ : binary	$i$ : injector
$F$ : fuel	$m$ : turbulent mixing
$f$ : frozen mixing	$o$ : reference quantity
$g$ : gas in rocket chamber	$ox$ : oxidizer
$K$ : Kolmogorov	$q$ : quenching

SPC 02-4034  
Contract Order Number FA8655-02-M034

*r*: reforming gas

*ref*: reforming

*st*: at stoichiometric condition

*w*: wall

*wg*: wall - combustion gas interface

*wr*: wall - reforming gas interface

## Part I

# Scaling and Performance Enhancement

## 1 Introduction

The definition of micropulsion keeps changing with the introduction of smaller and smaller thrust devices. Until 15 years ago "micro" means typically thrust  $\sim O(1) N$ , now commonplace for NSSK duties on satellites. A more current definition would classify now as "micro" thrusts of order  $O(1) \mu N$  to  $O(1) mN$ . Surveys of this propulsion area have appeared already [1, 2, 3].

Microthrusters are associated with the emergence of micro- and nano-satellite concepts, in which satellites are conceived capable of the same or similar performance of conventional satellites within a much smaller package/weight by using MEMS technology. Because of this new technology, new classes of small to ultra-small satellites are being envisaged [4, 5, 6], all of which must have thrusters for attitude control or for orbital changes. A host of new satellite concepts has been generated based on this premise, and mention of microsatellites 'swarms', or 'constellations', or 'clusters' can be found often in the specialized press. 'Platoons', 'formation flying' are also terms that can be found in common parlance, especially in the military press. A comprehensive description of the strategy, pluses and minuses and convenience of this concept is in [7]. In essence, the case is being made for clusters of simple satellites each much simpler, more reliable and especially cheaper than a single satellite embodying the total cluster capability.

A primer on MEMS technology is in [8, 9], which describes its history, micro-fabrication, materials, trends and industrial applications; articles on MEMS have also appeared [10] that have contributed to popularize it, showing striking pictures of micromachined gears, turbines and valves. Valves are ubiquitous critical MEMS components in many micro-thruster concepts, and much experimental/testing work is under way [11, 12, 13, 14].

Least be thought otherwise, MEMS is a concept and a technology applicable to most or all propulsion systems, subject to restriction(s) posed by physical laws to geometric scaling down. This fundamental aspect of MEMS has been, in fact, barely analyzed. The case for MEMS applied to [chemical] propulsion is based on scaling laws: thrust T scales with area (e.g., recall the rocket formula  $T = C_F P_C A_t$ , where the symbols stay for thrust coefficient, chamber/stagnation pressure, and throat area), while weight W scales with volume. Thus shrinking a chemical rocket engine will increase the T/W ratio, a very attractive trend. With caveat, the same trend applies to most electric thrusters, but not to electrodynamic tethers, to mention a counterexample. Hence, micropulsion has a ready-case made for itself based on T/W ratios. However, the scaling laws hold also throughout the range of physical effects that contribute to the working of a complete thruster system. This means, for instance, that viscosity

will play a much larger role as size gets smaller, and the simple isentropic expansion expressions utilized in conventional rocket engine design apply less and less as the dimensions shrink: in fact, measured  $I_{sp}$  of rocket micronozzles goes down by a factor 10 when the nozzle Reynolds Number  $Re$  drops (with size) from 4000 to 400 [15]. Similar performance degradation was measured in small (but not micro-) experimental resistojets [16] with Area Ratio = 100 and  $Re$  = 200-300: the  $I_{sp}$  were measured to be of order 70 s rather than the 130 s predicted by the classic 1-D formula. This fact was instrumental in determining the fate of the HmNT (Hydrazine MilliNewton Thruster) designed at JPL to despin a future Europa mission probe, since the conventional 1-D scaling from 1 N to 20 mN based on [17] did not work.

Actual simulation of nozzles using both Navier-Stokes and DMC simulations were performed recently [18] to assess quantitatively the effect of real gas physics on MEMS-fabricated flat nozzle performance. The results indicate the flow inside such flat nozzles is truly 3-D and that a flat nozzle, e.g., that in [19] has about 20% less thrust than a 2-D axisymmetric nozzle.

What all this means is that using MEMS for microthrusters must be complemented by the willingness to rework or adapt the physics associated to the new scales. This is by no means obvious to many of the researchers working in this area (e.g., in [20, 19] the authors do not even mention loss of performance due to viscous effects in microchemical rockets]. In fact, papers discussing these issues in some depth are few and very recent [31, 32, 35, 36, 37]. In these works viscous momentum, heat transfer and ionization effects are scaled (but not combustion physics). For future missions where micropulsion is a must, picking the 'right' physics will simplify design and avoid costly disappointments. In essence, a sensible strategy should not be to pick a thruster, scale it down and then check whether performance is good as in the original sample; rather, it should start by picking which physical effects need to be kept in and which discarded under the new small scale conditions, and only then modeling (or re-modeling) should start.

The purpose of this Part is to outline scaling effects when conventional chemical rockets are reduced in size, emphasizing effects due to combustion and heat transfer. The following analysis is rather crude, based as it is on the simple 1-D isentropic relationships describing rocket engine performance and on 1-D flame structure physics.

## 2 Scaling and Transport Equations

The reactive Navier-Stokes equations apply together with their boundary conditions ( $BCs$ ). Their nondimensional form is, for instance, in [23]. The well known viscosity and chemical source terms effects scale as the Reynolds ( $Re$ ) and Damköhler ( $Da$ ) numbers, respectively. In large enough engines the regime is in fact turbulent, so that instead of a  $Re$  and a  $Da$  number,  $Re$  and  $Da$  spectra should be considered.

The  $BCs$  can also be nondimensionalized, showing the importance of radiative effects. The most important  $BC$  is that for the energy at the walls, cast in terms of

energy fluxes.

As the characteristic engine size  $D$  shrinks, the ratio between surface  $\sim D^2$  and volume  $\sim D^3$  tends to grow, subtracting more and more of the chemical heat release through the combustion chamber walls. Walls become critical regions of the engine.

### 3 Scaling: Performance

In this section we are interested in finding the effect of scale (size)  $D$  on performance.

Assuming in a microrocket  $D/L$  is  $O(1)$ , the total power generated inside the rocket chambers scales as

$$W_{TOT} = W_{SP} \frac{\pi D^2 L}{4} \sim A_1 D^3 \quad (1)$$

with  $A_1 = \pi W_{SP}/4$ .

The power lost to the walls (by convection only) scales as

$$W_{TRANS} = h\pi DL(T_g - T_w) = A_2 D(T_g - T_w) \sim A_3 D^{3/2}(T_g - T_w) \quad (2)$$

with  $A_2 = \pi\kappa Nu \sim \pi\kappa Pr^{1/3} Re^{1/2} = \pi\kappa Pr^{1/3}(\rho U/\mu)^{1/2} D^{1/2} = A_3 D^{1/2}$  and  $A_3 = \pi\kappa Pr^{1/3}(\rho U/\mu)^{1/2}$ . This implies that the flux  $W_{TRANS}/D^2$  increases with decreasing  $D$ :

$$\frac{W_{TRANS}}{D^2} \sim A_3 \frac{T_g - T_w}{D^{1/2}} \quad (3)$$

Thus shrinking the size of the thruster results in higher and higher thermal loads on the chamber walls; they will tend to become hotter and hotter. A better analysis should include the radiative HT in series to the convective  $W_{TRANS}$ : at relatively larger  $D$  the “bottleneck” will be radiative, smaller  $D$  will switch control of HT to convection.

When steady-state is reached during the rocket operation the difference between (1) and (2) is the effective propellants heating power [24], scaling as

$$W_{TOT} - W_{TRANS} \sim \dot{m} C_p (T_g - T_i) \sim A_4 (T_g - T_i) D^2 \quad (4)$$

with  $A_4 = \rho U \pi / 4$ .

From (1), (2) and (4) the chamber stagnation temperature  $T_g$  will scale as

$$T_g \sim \frac{A_1 D^{3/2} + A_3 T_w + A_4 T_i D^{1/2}}{A_3 + A_4 D^{1/2}} \quad (5)$$

showing that in the limit  $D \rightarrow 0$  the  $T_g \rightarrow T_w$ .

The  $W_{TRANS}$  depends on  $Nu$ , i.e., on  $Re$  and  $Pr$ . The  $Re$  and  $Pr$  numbers in the chamber scale, see (15), as

$$Re \sim \frac{1}{\mu_o \left( \frac{T_g}{T_o} \right)^{2/3} R} \frac{p}{T_g} \frac{UD}{T_g} \sim \frac{T_o^{2/3}}{\mu_o} \frac{p}{R} UD \left( \frac{A_1 D^{3/2} + A_3 T_w + A_4 T_i D^{1/2}}{A_3 + A_4 D^{1/2}} \right)^{-5/3} \quad (6)$$

and

$$Pr \sim \frac{\mu_o}{\kappa_o} C_p(T_g) \quad (7)$$

where the quantities with the index  $_o$  are some reference quantities. Therefore

$$Nu \sim \left(\frac{p}{R} U\right)^{1/2} D^{1/2} \left(\frac{A_1 D^{3/2} + A_3 T_w + A_4 T_i D^{1/2}}{A_3 + A_4 D^{1/2}}\right)^{-5/6} \left(\frac{T_o^2}{\kappa_o^2 \mu_o}\right)^{1/6} C_p(T_g)^{1/3} \quad (8)$$

$T_g$  affects thrust  $F$ . The effective thrust  $F$  will scale (ideally!), see (15), as

$$F = \dot{m} V_e = \rho U \pi \frac{D^2}{4} \sqrt{\frac{2\gamma \mathfrak{R}_u}{\gamma-1} \frac{T_g}{M_W} \left[1 - \left(\frac{P_e}{P_o}\right)^{(\gamma-1)/\gamma}\right]} \sim \quad (9)$$

$$\sim A_5 D^2 T_g^{1/2} \sim A_5 D^2 \left(\frac{A_1 D^{3/2} + A_3 T_w + A_4 T_i D^{1/2}}{A_3 + A_4 D^{1/2}}\right)^{1/2}$$

with  $A_5 = \rho U \pi / 4 \sqrt{\frac{2\gamma \mathfrak{R}_u}{\gamma-1} \frac{1}{M_W} \left[1 - \left(\frac{P_e}{P_o}\right)^{(\gamma-1)/\gamma}\right]}$  ( $\mathfrak{R}_u$  is the universal gas constant and  $M_W$  is the molecular weight): Therefore, the thrust scales with a power  $\sim 5/2$  of the size  $D$ . This implies a drastic reduction of thrust as  $D$  shrinks.

In large boosters or space launchers the engine walls are regeneratively cooled by the propellants to reduce the thermal load. Upper stage or kick-stage *LRE* are typically radiatively cooled, avoiding complex cooling systems altogether. This may result in loosing too much power as  $D$  shrinks; therefore it may be useful to look for alternatives.

One alternative might be endothermic reforming of the primary fuel, or propellant. Reforming of Liquid HydroCarbon fuels (*LHC*) produces  $H_2$ ,  $CO$  and other *HC* species (it may also produce soot). Reforming is endothermic, but reforming products raise the  $T_i$  thus compensating, partly, for the reduction of  $F$ , see (9). An additional benefit may possibly accrue by using dense, storable *LHC* as fuel. With reforming the global energy balance of the engine becomes:

$$W_{TOT} - \dot{Q}_{ref} = \dot{m}_F C_{p_F} (T_g - T_i) \quad (10)$$

where  $\dot{Q}_{ref}$  scales  $\sim DL \sim D^2$  and  $Nu$  just as  $W_{TRANS}$ . However, the reformed fuel produces new reactants (e.g.,  $CO$  and  $H_2$ , when reforming methanol, see [19]) at much higher  $T_i$  [25]. Therefore, part of the  $W_{TRANS}$  is recovered in the form of higher enthalpy reactants, while excessive *HT* fluxes due to the increasing  $Nu$  with decreasing  $D$  are automatically compensated.

### 3.1 Thrust Analysis

To conclude our scaling analysis of Part 1 on microthrusters, we want to show the effect of thruster size  $D$  and of flow Reynolds number  $Re_D$  on thrust  $F$ . The Reynolds

number tell us if the flow is turbulent or not. The ideal thrust is

$$F = \dot{m}V_e = \rho U \pi \frac{D^2}{4} \sqrt{\frac{2\gamma \mathfrak{R}_u}{\gamma - 1} \frac{T_g}{M_W} \left[ 1 - \left( \frac{P_e}{P_o} \right)^{(\gamma-1)/\gamma} \right]} \quad (11)$$

( $\dot{m}$  is the mass flow rate,  $V_e$  is the velocity at the nozzle exit,  $\rho$  is the density,  $U$  is the velocity,  $\gamma$  is the specific-heat ratio,  $\mathfrak{R}_u$  is the universal gas constant,  $M_W$  is the molecular weight,  $T_g$  is hot gas temperature in the chamber,  $P_e$  is the pressure at the nozzle exit and  $P_o$  in the chamber). We manipulate this expression assuming  $D$  and  $Re_D$  as variables

$$F = \frac{\pi}{4} \mu T_g^{1/2} Re_D D \sqrt{\frac{2\gamma}{\gamma - 1} \frac{\mathfrak{R}_u}{M_W} \left[ 1 - \left( \frac{P_e}{P_o} \right)^{(\gamma-1)/\gamma} \right]} \quad (12)$$

Since the viscosity  $\mu$  is function of temperature,  $\mu \sim \mu_o (T_g/T_o)^{2/3}$ , we have

$$F = \frac{\pi}{4} \frac{\mu_o}{T_o^{2/3}} T_g^{7/6} Re_D D \sqrt{\frac{2\gamma}{\gamma - 1} \frac{\mathfrak{R}_u}{M_W} \left[ 1 - \left( \frac{P_e}{P_o} \right)^{(\gamma-1)/\gamma} \right]} \quad (13)$$

where  $1 - (P_e/P_o)^{(\gamma-1)/\gamma}$  is the ideal thermodynamic efficiency that quantifies the effects of the nozzle pressure ratio  $P_e/P_o$  and the specific-heat ratio  $\gamma$  upon  $V_e$ . In the following analysis we assume that this efficiency is 0.65, corresponding to  $P_e/P_o \sim 100$  and to an exit-throat area ratio  $A_e/A_t \sim 15$ ; these are common values in chemical microthrusters [30]. We assume also  $\gamma = 1.3$ ,  $R_g = \mathfrak{R}_u/M_W = 280 \text{ J/(kg K)}$ ,  $\mu_o \sim 10^{-5} \text{ kg/(m s)}$ ,  $T_o = 300 \text{ K}$ ,  $T_g = 1600 \text{ K}$ .

We know that at small Reynolds number [31, 32] viscous losses cannot be neglected. Therefore we included a factor,  $\eta_\mu$ , linearly varying with the Reynolds number, that is unity at  $Re_D = 10^4$  and 0.8 at  $Re_D = 10^2$  and below:

$$\eta_\mu = 2 \cdot 10^{-5} (Re_D - 100) + 0.8 \quad (14)$$

Although crude, this procedure does account for viscous losses otherwise hard to account for without at least  $2 - D$  numerical calculations.

Finally we obtain the effective thrust shown in Fig. 1. Results are in agreement with performance of chemical thrusters found in literature [30]. In particular, we note that to have a certain thrust  $F$  (i.e., moving along an iso-thrust line in Fig. 1), we need a higher Reynolds number at smaller scales; moreover, to increase thrust we must increase the Reynolds number  $Re_D$  much more at small scales than at large scales. For example, if we want to increase thrust from  $F \approx 0.3 \text{ N}$  up to  $F \approx 0.6 \text{ N}$ , for a  $0.0075 \text{ m}$  diameter thruster we need to increase the Reynolds number from  $\approx 1300$  up to  $\approx 2500$ , meaning a  $\Delta Re_D \approx 1200$ ; for a  $0.0025 \text{ m}$  diameter thruster we need to increase the Reynolds number from  $\approx 3700$  up to  $\approx 7000$ , meaning a  $\Delta Re_D \approx 3300$ . Moreover, assuming a constant Reynolds number, to increase the thrust we

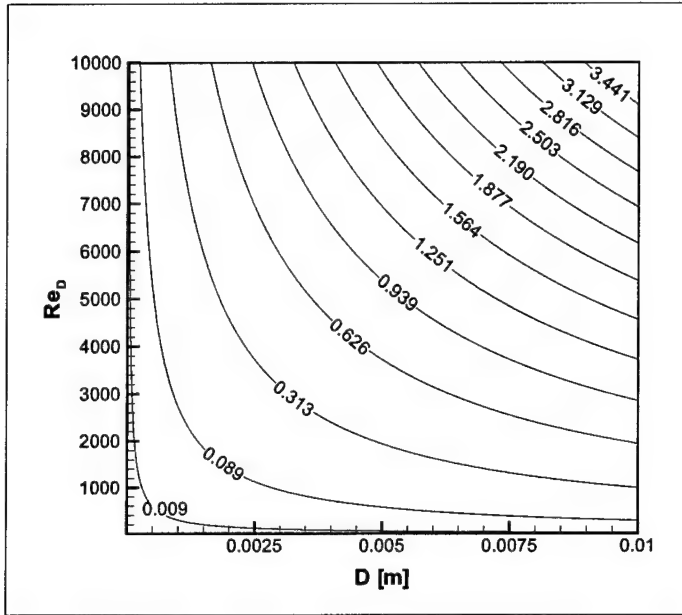


Figure 1: Effective thrust (in N) map as function of the thruster size and chamber Reynolds number.

must enlarge the thruster much more at lower  $Re_D$  than at higher  $Re_D$ . Therefore, it is convenient to work at high Reynolds number inside the chemical microthruster. High thrust at small scales means managing turbulent flows, stressing the importance of turbulent combustion analysis at small scales. A practical way to increase  $Re_D$  is to increase the pressure and not the flow velocity, since this last would make flame stabilization more critical.

### 3.2 Chamber Temperature Analysis and Effect of Reforming

In Part 1 we obtained that the chamber stagnation temperature  $T_g$  scales as

$$T_g \sim \frac{A_1 D^{3/2} + A_3 T_w + A_4 T_i D^{1/2}}{A_3 + A_4 D^{1/2}} \quad (15)$$

where  $A_1 = (\pi/4)^2 \rho \Delta H_R U D^{-1}$  ( $\Delta H_R$  is the reaction heat),  $A_3 = \pi \kappa Pr^{1/3} (\rho U / \mu)^{1/2}$  ( $\kappa$  is the thermal conductivity,  $Pr$  is the Prandtl number),  $A_4 = \rho U \pi / 4$ .  $T_w$  is the wall temperature and  $T_i$  is the inlet temperature of reactants. Substituting we have

$$T_g \sim \frac{\frac{\pi}{4} \Delta H_R D^{1/2} + 4 \kappa Pr^{1/3} (\rho U \mu)^{-1/2} T_w + C_p T_i D^{1/2}}{4 \kappa Pr^{1/3} (\rho U \mu)^{-1/2} + C_p D^{1/2}} \quad (16)$$

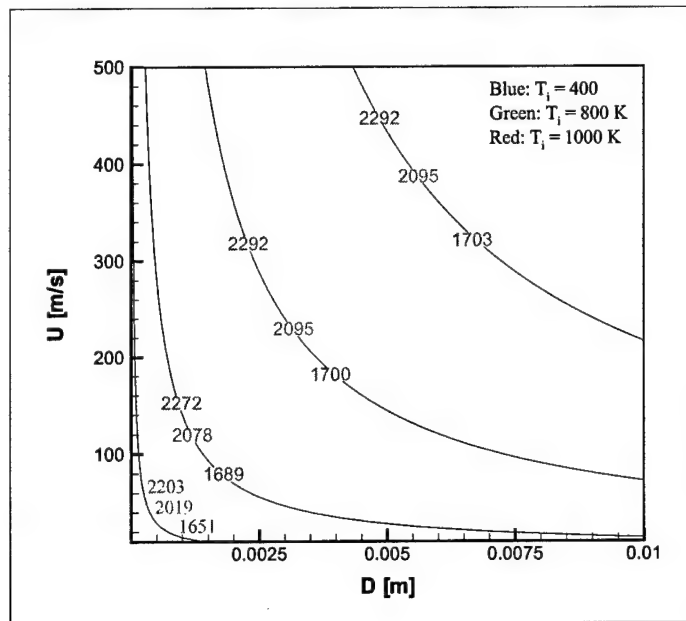


Figure 2: Hot gas temperature  $T_g$  map (in  $K$ ) as function of the thruster size and chamber velocity (up to 500  $m/s$ ).

We assume, for instance,  $\Delta H_R = 2 \cdot 10^6 \text{ J/kg}$ ,  $T_w = 1000 \text{ K}$ ,  $\kappa = 0.01 \text{ W/(m K)}$ ,  $Pr = 1$ ,  $\rho = 1$ ,  $C_p = 1200 \text{ J/(kg K)}$ . With these assumptions and considering three temperatures for the inlet reactants ( $T_i = 400, 800, 1000 \text{ K}$ ),  $T_g$  varies as shown in Fig. 2 and 3; in these Figures each iso- $T_g$  line corresponds to three  $T_g$  levels, associated to the three inlet temperatures assumed. We considered the velocity instead of the Reynolds number, because using  $Re_D$  the size  $D$  would disappear from the  $T_g$  expression.

Higher inlet temperatures  $T_i$  corresponds to reformed reactants assumed as fuel. Increasing  $T_i$  implies to raise the chamber temperature  $T_g$ ; if we want to operate the engine at constant wall temperature  $T_w$ , we must improve cooling. We note that iso- $T_g$  lines in Fig. 2 and 3 have higher  $\Delta T$  for higher  $T_i$ , when decreasing the thruster size  $D$ . Moreover, at small scales, once the size  $D$  is fixed, the effect of flow velocity  $U$  on  $T_g$  decreases; it means that the heat transfer to the walls at small thruster size is controlled mostly by the size  $D$  itself and not by the velocity. A more detailed analysis will consider the dependence of  $T_w$  and  $T_i$  on  $T_g$ .

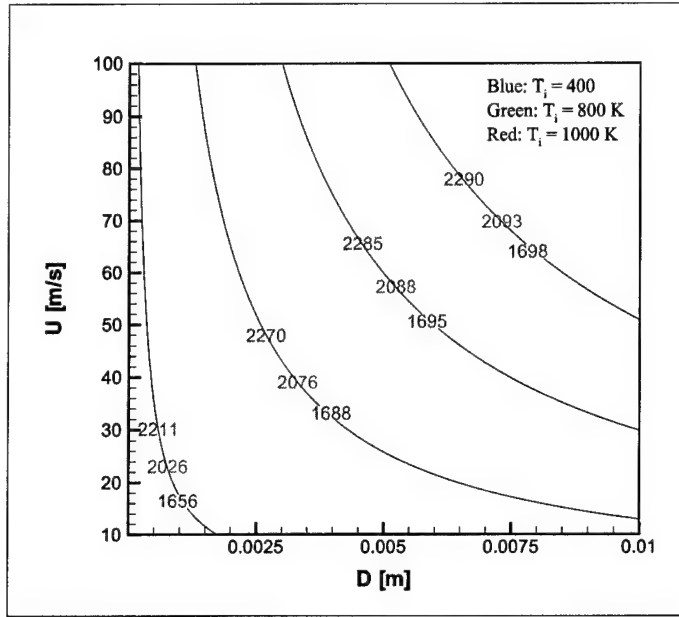


Figure 3: Hot gas temperature  $T_g$  map (in K) as function of the thruster size and chamber velocity (up to 100 m/s).

#### 4 Scaling: Turbulent Mixing and Combustion

Inside the rocket chamber reactants [reformed or not] mix and burn. A characteristic injector size  $d \sim D/m$  ( $m \gg 1$ ) may be defined.

The factor  $m$  depends on the mixing length  $l_m$  of the nonpremixed flame issuing from the injector. As a first approximation [26]  $l_m$  scales as

$$l_m \sim (\varepsilon t_{ch}^3)^{1/2} \quad (17)$$

In nonpremixed flames the chemical time  $t_{ch}$ , is effectively controlled by stoichiometry, i.e.,  $Z_{st}$ , and strain  $\chi$  in the  $Z \approx Z_{st}$  region:

$$t_{ch} = \frac{Z_{st}^2(1 - Z_{st})^2}{\chi_{st}} \quad (18)$$

Still from [26], the mean value of  $\chi_{st}$  is  $\sim 2 \left| \nabla Z \right|_{st}^2 D_{st}$ .

Then

$$t_{ch} \sim \frac{Z_{st}^2(1 - Z_{st})^2}{2 \left| \nabla Z \right|_{st}^2 D_{st}} \sim A_6 d^2 \sim \frac{A_6}{m^2} D^2 \quad (19)$$

This results in a mixing length

$$l_m \sim \varepsilon^{1/2} \left( \frac{A_6}{m^2} \right)^{3/2} D^3 \quad (20)$$

decreasing rapidly with  $D$ .

In fact, since  $\varepsilon \sim U^3/D$ , and the relationship between  $d$  and  $D$  is given (see (1)) by the balance

$$\rho U_i \pi \frac{d^2}{4} Q_{comb} = W_{TOT} \sim A_1 D^3 \quad (21)$$

where  $\rho U_i$  is the mass flow rate of reactants, and  $Q_{comb}$  is the heat of combustion for unit reactant mass. For fixed  $\rho U_i$ ,  $d^2 \sim A_7 D^3$ , with  $A_7 = 4 A_1 D^3 / (\rho U_i \pi Q_{comb})$ , and therefore

$$d^3 \sim A_7^{3/2} D^{9/2} \quad (22)$$

Thus

$$l_m \sim \frac{U^{3/2}}{D^{1/2}} A_6^{3/2} A_7^{3/2} D^{9/2} \sim U^{3/2} D^4 (A_6 A_7)^{3/2} \quad (23)$$

i.e., the mixing length  $l_m \sim U^{3/2} D^4$  decreases even more rapidly with  $D$  than indicated by (20). Therefore, provided the regime remains turbulent, the mixing length will decrease faster than the chamber size. The injector size  $d$ , from equation (22), scales as  $D^{3/2}$  ( $d \sim A_7^{1/2} D^{3/2}$ ); if mixing must take place within the chamber length  $L \sim D$ , i.e.,  $l_m < D$ , this translates into the constraint

$$D^4 (A_6 A_7)^{3/2} U^{3/2} < D \Rightarrow d < (A_6^3 A_7 U^3)^{-1/4} \quad (24)$$

This constraint may produce injectors with such small  $Re$  that the discharge coefficient becomes too small. So, this may be a severe constraint on operability of microrockets.

## 4.1 Quenching

Combustion at sufficiently large  $Re$  will be in the laminar flamelet regime, since diffusion coefficients scale as  $1/p$ , while chemical kinetics scales as  $p^n$ , with the exponent  $n$  between 1 and 2. The  $Re$  number of the injector scales with  $d$ , but since  $\rho U_i D^2$  is approximately  $\rho_g U D^2$ , the chamber Reynolds number and the injector  $Re$  will be of the same order. In the flamelet regime the local energy balance is dominated by interaction between local kinetics heat release (the source) and the flame stretch effect that subtracts part of this heat release in the form of heat convected away by local turbulent structures (the sink).

Quenching occurs when the Karlovitz number defining the ratio between the chemical time associated to the local turbulent flame structure and the strain time  $\chi^{-1}$  ( $\sim \partial u / \partial x \sim U_i / d$  as a first approximation) becomes  $\sim O(1)$ .

In fact, the turbulent spectrum generates a strain spectrum. The scales of turbulence in mixing and combustion may be crudely estimated using the injector  $Re_i$ :  $\varepsilon_i \sim U_i^3 / d$  and  $l_{K_i} \sim d \cdot Re_i^{-3/4}$ , and accounting for the fact that the fuel may be at a temperature much higher than the oxidizer in the case of reforming.

The higher  $\chi$  will occur at the smaller scales, in between  $d$  and  $l_{K_i}$ .

To estimate Karlowitz, the chemical time,  $t_{ch}$ , for a simple 1-step reaction of order  $n$  scales as  $t_{ch} \sim A^{-1} \rho^{1-n} \text{Exp}[E_a/RT_g]$  and, using (15),

$$t_{ch} \sim A^{-1} \rho^{1-n} \text{Exp} \left[ \frac{E_a (A_3 + A_4 D^{1/2})}{R (A_1 D^{3/2} + A_3 T_w + A_4 T_i D^{1/2})} \right] \quad (25)$$

The stretch spectrum is

$$\chi \sim \frac{\partial u}{\partial \lambda} \quad (26)$$

where  $\lambda$  is the local turbulent scale. As a first approximation, simple Kolmogorov scaling yields  $\varepsilon \sim u^3/\lambda \sim U^3/D$ , from which

$$\chi \sim \frac{\partial u}{\partial \lambda} \sim \frac{\varepsilon}{u^2} \sim \frac{\varepsilon}{KE} \sim \frac{U^3}{D \cdot KE} \quad (27)$$

with KE the local turbulent kinetic energy.

Quenching may occur if  $Ka \geq 1$ , i.e., when

$$\frac{1}{KE} \frac{U^3}{D} A^{-1} \rho^{1-n} \text{Exp} \left[ \frac{E_a (A_3 + A_4 D^{1/2})}{R (A_1 D^{3/2} + A_3 T_w + A_4 T_i D^{1/2})} \right] \geq 1 \quad (28)$$

that scales with  $D$  in a complex way. In fact, for large enough  $D$ , stretch may not matter, since  $E_a$  is typically large. However, when  $D$  is reduced the gradual reduction of  $T_g$  slows down kinetics until quenching occurs. Expression (29) shows the beneficial effect of reforming, which increases  $T_i$  and affects positively (and exponentially) quenching. Eventually, however, as  $D$  shrinks, the ratio between flamelet thickness  $t_F$  and  $D$  becomes  $\sim O(1)$ , and combustion becomes impossible. Said otherwise, residence time/chemical time (i.e., the global engine Damköhler number) must remain  $> 1$  for the propellants to burn. This is to be taken as the absolute minimum size criterion: in fact, at this point the very existence of a flame will be impossible. Long before this, however, the flame regime will have already become laminar.

## 5 Scaling: Laminar Combustion

Shrinking enough  $D$  means that the ratio  $L_K/D \sim Re^{-3/4}$  between chamber Kolmogorov scale and size tends to 1: the regime will eventually become laminar. No spectrum of scales exists any longer. The flame may be quenched by wall HT if the chamber radius  $D/2$  is roughly of the same order as the quenching distance  $d_q$  that can be estimated by [27]

$$d_q \sim A_8 \frac{T_{g,lean}}{T_g} \frac{T_g - T_i}{T_g} \frac{\kappa}{\rho C_p S_L} \quad (29)$$

dominated, in this extreme case, by the effect of the flame temperature  $T_g$ , lowered by the wall HT. Thus for combustion to exist in this regime the condition

$$\frac{D}{d_q} \gg 2 \quad (30)$$

must be satisfied. This situation is extreme, as the nozzle will also be dominated by viscous effects greatly degrading its performance. Even in the case  $D \gg d_q$  asymptotic analysis [23] predicts extinction due to laminar strain when the so-called reduced Damköhler number  $\delta$ , defined as

$$\delta = \frac{Y_{ox} A \text{Exp}[-E/RT_{st}]}{2\rho D_{12} (\nabla Z_{st})^2 Z_{st} \beta^3} \quad (31)$$

where  $\beta$  is the Zeldovich number

$$\beta = \frac{E(T_{st} - T_{f,st})}{2Z_{st}(1 - Z_{st})RT_{st}^2} \quad (32)$$

becomes  $< 1$  (actually,  $< 1 - \xi$ , where  $\xi$  depends on  $Z_{st}$  and on the ratio between temperature increase due to combustion and temperature difference between fuel and oxidizers burned; typically,  $\xi < 1$ , but this may change to some extent in the case of reforming, see [23]). This may occur when  $D$  becomes so small that the reaction rate (the numerator of  $\delta$ ) becomes too small because the  $T_g$  ( $= T_{st}$ ) drops too much due to wall heat transfer. As a rough approximation Equation (15) can be used to define the scaling of  $\delta$  with  $D$  and to therefore check when it becomes  $< 1$  leading to extinction.

## 6 Conclusions

In this first Part we have tried to outline a first set of scaling rules that will apply to (most) LRE.

Chemical microrocket technology should include preliminary design considerations based on scaling as the size of rocket engines is reduced. The  $D^{3/2}$  effect dominating heat release/heat transfer can be partially compensated by reforming of fuel (e.g., using methanol as fuel), since the heat lost through the engine walls is partially recuperated in the form of higher temperature reactants. For fixed energy density there are no scaling limits posed by turbulent mixing length per se, but there are definite limits imposed by discharge coefficients, and also by flame stretch, that will lead to quenching. As  $D$  shrinks, flame stretch subtracts energy faster and faster, making flame quenching possible at small scales. Reforming may help in this regime as it raises fuel (or propellants) temperatures, and accelerates kinetics. Eventually, as the chamber of the microrocket shrinks, the regime of the injection system (and that inside the chamber) will become laminar, and quenching due to the BL will occur. The ultimate limit to size reduction is posed by the structure of the flame itself, that scales

indirectly with size through the reduction in flame temperature; in practical applications, however, this limit corresponds to thrust so small that other classes of thrusters may become far more appealing.

Concerning scaling, we focused on thrust and chamber temperature. In the thrust analysis we have included a factor taking into account viscous losses. For a fixed thrust, higher Reynolds numbers are needed at smaller scales; to increase thrust, we must increase the Reynolds number  $Re_D$  much more at small scales than at large scales. Assuming a constant Reynolds, to increase the thrust we must enlarge the thruster, much more at lower  $Re_D$  than at higher  $Re_D$ . To summarize, it is convenient to work at high Reynolds number inside chemical microthrusters. High thrust at small scales means managing turbulent flows and turbulent combustion at small scales. In this context, a practical way to increase  $Re_D$  is to increase pressure, not flow velocity, that instead would make flame stabilization more critical.

Finally, we performed a simplified analysis of inlet temperature  $T_i$  on chamber temperature  $T_g$ . Higher  $T_i$  corresponds to the case of reformed reactants as fuel. Increasing  $T_i$  implies to increase the chamber temperature  $T_g$ . We noted that at small scales, for a fixed  $D$ , the effect of flow velocity  $U$  on  $T_g$  decreases; it means that heat transfer to the walls at small thruster size is controlled by the size  $D$  itself and not by the velocity.

## Part II

# Methanol Cracking and Performance

## 1 Introduction

The requisite for lighter and lighter payloads for future space applications leads to onboard hydrocarbon reforming as an alternative to high hydrogen fuel tank volumes. The purpose of this Part is to analyse combustibles production from liquid hydrocarbon fuels. Reforming processes have been already proposed since they are known and tested [Ref. 29]. Cracking processes look however, much more advantageous than reforming, thanks to the smaller Gibbs energy required. For this reason cracking processes for micro propulsion applications are examined. The only reactant considered is methyl alcohol ( $\text{CH}_3\text{OH}$ ) because of its high condensation temperature (300 K at atmospheric pressure) and its low specific volume ( $V=1.25\times 10^{-3} \text{ m}^3/\text{kg}$ ). Besides, methyl alcohol is relatively inexpensive.

Effects of cracking or reforming on chamber temperature and performance have been included in the scaling analysis of Part I. In particular, we performed a simplified analysis of inlet temperature  $T_i$  on chamber temperature  $T_g$ . Higher  $T_i$  corresponds to the case of reformed reactants as fuel and implies to increase the chamber temperature  $T_g$ .

## 2 Chemical calculations

The schematic path of the reactants from tanks to combustion chamber outlet is reported in figure 1.

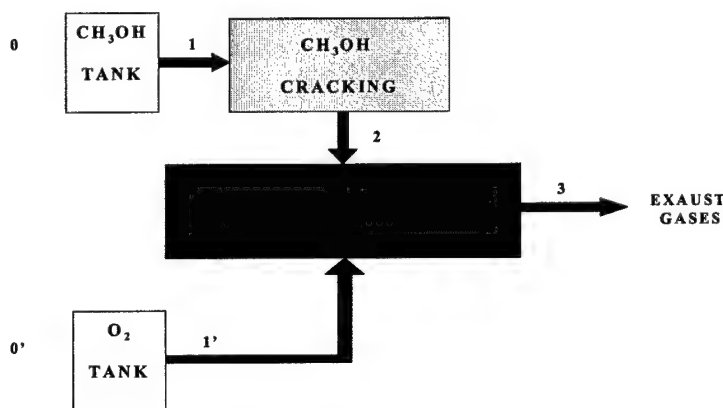


Figure 1 Schematic fuel path

To facilitate the figure comprehension, a short explanation follows:

- 0 - 1 → fuel path from the alcohol methyl tank to the inlet of the cracking chamber;
- 0 - 1' → oxygen path from its tank to the inlet of the combustion chamber;
- 1 - 2 → methanol cracking processes;
- 1' - 3 → combustion.
- 2 - 3 → combustion.

This figure shows that the inlet combustion chamber conditions should ideally correspond to those of the outlet products of cracking.

In the first section (1.1), the methanol cracking processes (step 1-2) are examined; in the following (1.2), the combustion is examined, (step 2-3, 1'-3). The analysis is performed for the time being and for simplicity, at equilibrium conditions both for the cracking processes and combustion. Kinetic calculations will be reported later.

## 2.1 Cracking: equilibrium analysis

The first part of the work consists in the equilibrium analysis of the cracked products obtained from cracking, by using the NASA's CEA600 equilibrium code [Ref. 28].

This code accounts cracking hydrocarbon products and includes also graphitic carbon species.

Initial conditions are investigated by varying initial temperature and pressure. The initial temperature is assumed equal to that of combustor walls; therefore it assumes values from 600K to 1200K. The cracking process is calculated assuming an thermodynamic isobaric transformation to focus on the exothermic or endothermic nature of the cracking process, depending on initial conditions.

Figures 2-5 show the trend of products versus pressure, at fixed (initial) temperature  $T_0=600K, 800K, 1000K, 1200K$ .

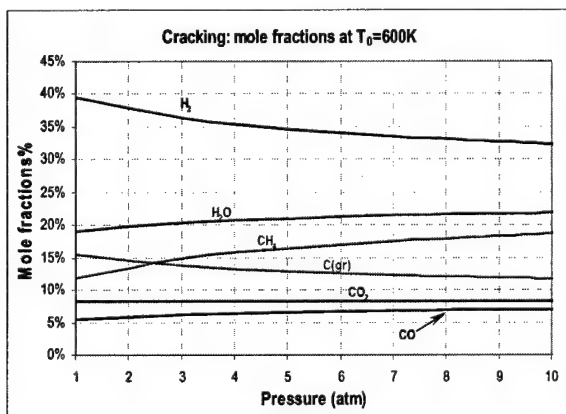


Figure 2 Mole fractions versus pressure at initial temperature ( $T_0=600K$ )

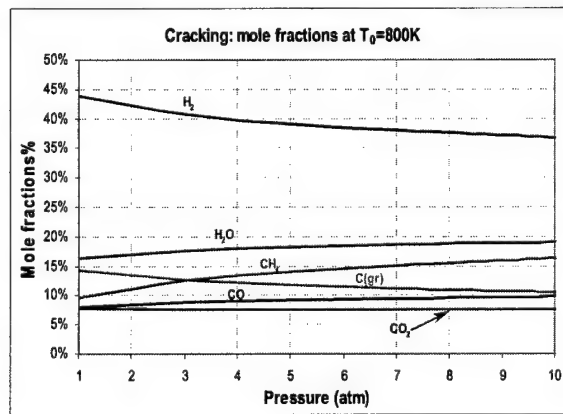


Figure 3 Mole fractions versus pressure at initial temperature ( $T_0=800K$ )

These figures show that methanol dissociates into light species such as molecular hydrogen, and methane, water, oxide carbon and monoxide carbon but also graphite.

The presence of this species suggest that, using realistic kinetics, soot might therefore be produced.

In order to maximize mole fractions of light products, low pressures must be used: in fact, the hydrogen mass fraction percent decreases with increasing pressure. This result could suggest to operate at lower pressures, but needs to be confirmed because obtained at equilibrium conditions (kinetic calculations will examine later on the influence of pressure on the ignition delay time, not taken into account so far). Furthermore, the products of cracking must be injected, inside the combustion chamber: therefore cracking must be done at pressure higher than combustor pressure.

The comparison between figures 2-5 shows that as the temperature increases, the percentage of light products increases too. Molecular hydrogen grows by about 13% going from 40% at  $T_0=600\text{K}$  and  $P_0=1\text{atm}$  to 53% at  $T_0=1200\text{K}$  and  $P_0=1\text{atm}$ .

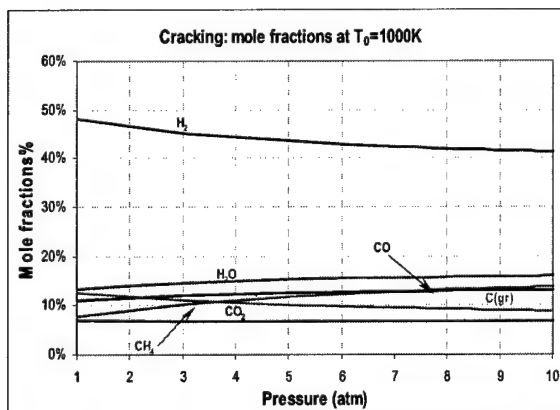


Figure 4 Mole fractions versus pressure at initial temperature ( $T_0=1000\text{K}$ )

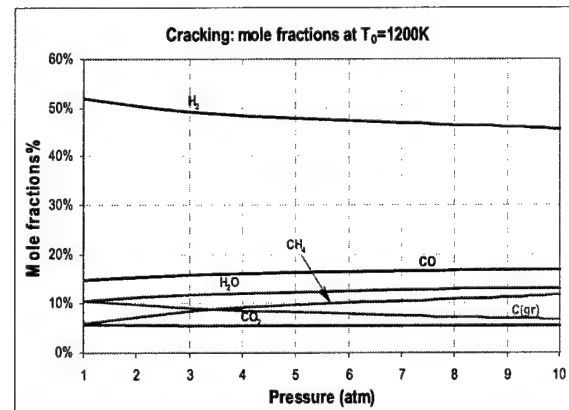


Figure 5 Mole fractions versus pressure at initial temperature ( $T_0=1200\text{K}$ )

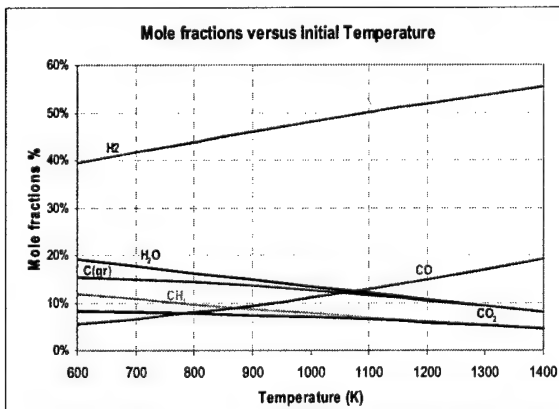


Figure 6 Mole fractions versus initial temperature at  $P=1\text{atm}$

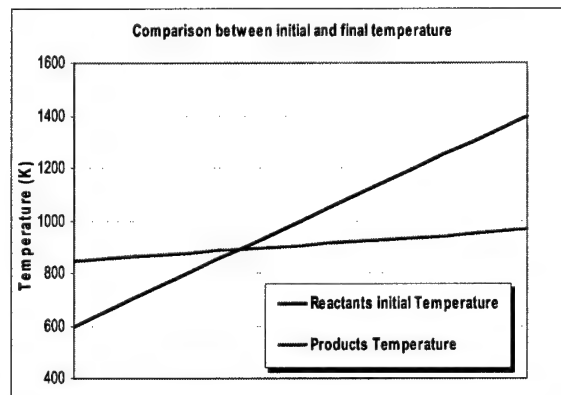


Figure 7 Comparison between final and initial temperature at  $P=1\text{atm}$

Mole fractions products versus initial temperature (at fixed pressure  $P_0=1\text{atm}$ ) are plotted in figure 6. This figure shows that different species mole fractions are produced at the different initial temperatures conditions. In fact, going to higher temperature, hydrogen and monoxide

carbon mole fractions increase; meanwhile graphitic and dioxide carbon mole fractions decrease. This explains the temperature trend plotted in figure 7.

Figure 7 also shows that, at  $P=1\text{atm}$ , and if the reactants initial temperatures is below  $T=910\text{K}$ , this process is exothermic, while, above this temperature, it becomes endothermic. This is due to the different heats of formation of hydrogen and carbon monoxide compared to graphitic and dioxide carbon species.

This confirms that above  $T=910\text{K}$  at  $P=1\text{atm}$ , or above  $T=986\text{K}$  at  $P=5\text{atm}$ , the methanol cracking process has an important combustor cooling role.

Figures 8-9 show methanol cracking performance at  $P=5\text{atm}$ . In this case the  $\text{H}_2$  mole fractions are smaller than  $P=1\text{atm}$  case. This fact partially explains the final cracking temperature higher at  $P=5\text{atm}$  than at  $P=1\text{atm}$ .

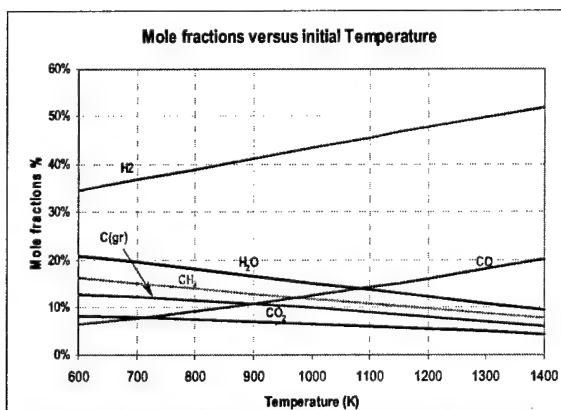


Figure 8 Mole fractions versus initial temperature at  $P=5\text{atm}$

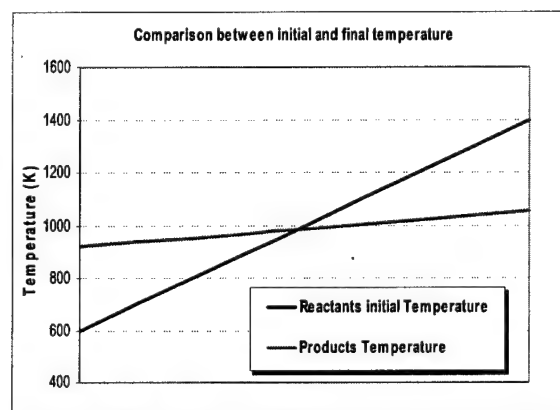


Figure 9 Comparison between final and initial temperature at  $P=5\text{atm}$

Figures 10-11 show methanol cracking performance at  $P=10\text{atm}$ .

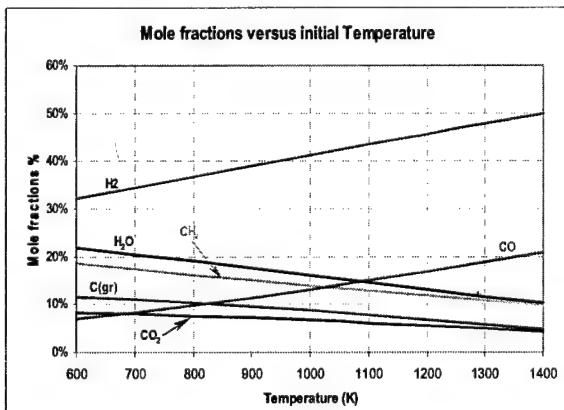


Figure 10 Mole fractions versus initial temperature at  $P=10\text{atm}$

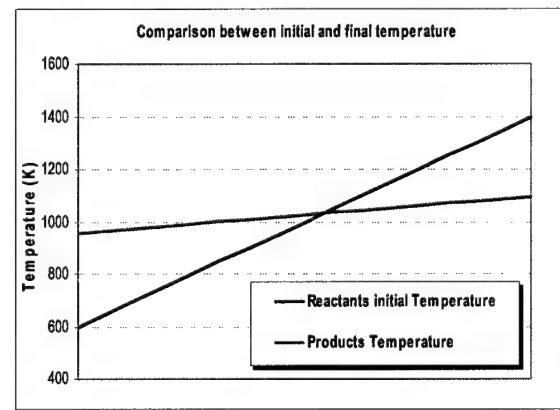


Figure 11 Comparison between initial and final temperature at  $P=10\text{atm}$

### 3 Equilibrium performance

The second part of this report contains an analysis of ideal rocket performance with 'cracked' fuel and oxygen.

A wide range of initial combustion chamber pressures and temperatures, and several values of the equivalence and expansion ratios are investigated.

The calculations are obtained by assuming as inlet combustor temperature and mole fractions, those already obtained. In particular, fixing the inlet cracking temperature at 1000K (this will be the ideal wall temperature), the fuel temperature at the combustor inlet is that calculated in the previous sections, i.e., the temperature at the outlet of cracking reactor. Thus the performance is calculated by assuming as initial values  $T_{\text{cracking}}^{(1)}=1000\text{K}$ , and  $P_{\text{cracking}}=1, 5$  and 10atm. The combustor pressures used to perform the calculations are also  $P_{\text{combustion}}=1, 5$  and 10atm. In fact, it must to be noted that the cracking temperature, i.e., the wall temperature, is strongly dependent on that of combustion. In turn, this depends on the fuel mass fraction: this means that all quantities are linked. This coupling will be taken into account later.

The specific impulse, thrust coefficient, temperature and mole fractions trends plotted in figures 12-14 are obtained at the following conditions:

CRACKING	COMBUSTION
$T_{\text{cracking}}^{(1)} = 1000\text{K}$	$T_{\text{combustion}}^{(2)} = 905.17\text{K}$
$T_{\text{cracking}}^{(2)} = 905.17\text{K}$	$P_{\text{combustion}} = 1\text{atm}$
$P_{\text{cracking}} = 1\text{atm}$	$Ae/At = 10$

Table 1

varying the equivalence ratio ( $\Phi$ ).

The apex refers to the inlets or outlets reported in figure 1. Thus,  $T_{\text{cracking}}^{(1)}$  indicates the reactant temperature at point 1, and so on.

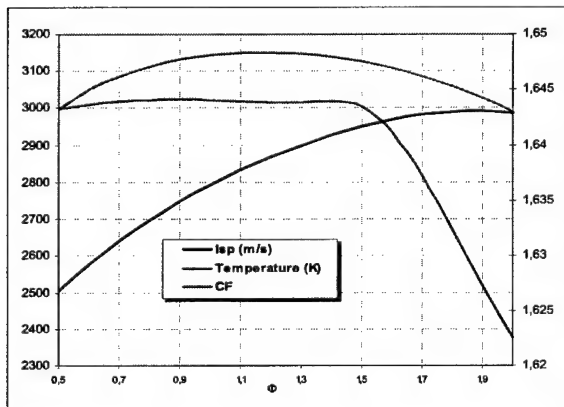


Figure 12  $P_{\text{combustion}}=1\text{atm}$ ,  $T_{\text{combustion}}=905.17\text{K}$ ,  $Ae/At=10$

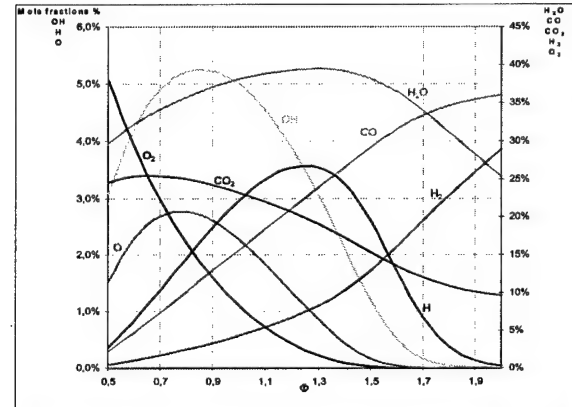


Figure 13  $P=1$   $P_{\text{combustion}}=1\text{atm}$ ,  $T_{\text{combustion}}=905.17\text{K}$ ,  $Ae/At=10$

Figure 12 shows a weak dependence of the thrust coefficient CF on equivalence ratio: CF is about constant at 1.643 until  $\Phi=1.5$ ; above it, it decreases to 1.6225. The specific impulse increases from 2500m/s to 3000m/s with equivalence ratio, reaching a maximum at  $\Phi=1.9$ . The combustor chamber temperature reaches a peak ( $T=3150K$ ) at  $\Phi=1.1$ , dropping after this to 3000K.

The specific impulse and CF trends can be explained by their analytic expressions. For instance, the ideal specific impulse expression is:

$$Isp = \left[ \frac{2}{g} \frac{\gamma}{\gamma-1} \frac{\bar{R} T_{comb}}{M} \left( 1 - \frac{p_e}{p_c} \frac{\gamma-1}{\gamma} \right) \right]^{\frac{1}{\gamma}} \quad (1)$$

As a consequence, the maximum specific impulse lies at a mixture ratio  $\Phi=1.9$ , i.e. between the mixture ratios of minimum molecular weight and maximum combustion temperature (see fig.14).

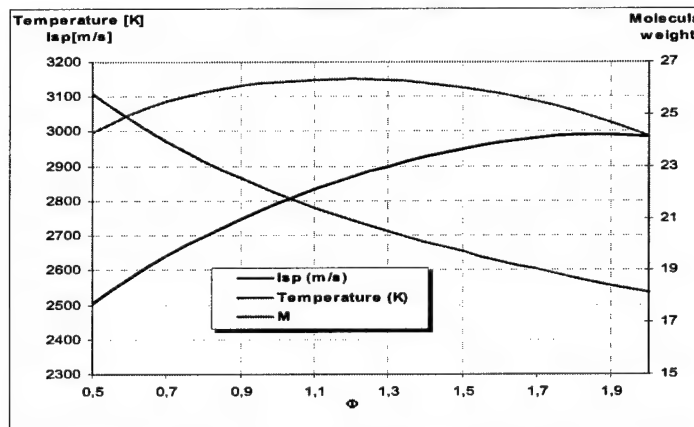


Figure 14  $P_{combustion}=1\text{atm}$ ,  $T_{combustion}=905.17\text{K}$ ,  $A_e/A_t=10$

The ideal CF expression (2) points out its dependence on  $\gamma$ ,  $p_e/p_c$ , and  $A_e/A_t$ , not on combustor temperature:

$$CF = \frac{F}{p_e A_t} = \gamma \left( \frac{2}{\gamma+1} \right)^{\frac{\gamma+1}{2(\gamma-1)}} \left\{ \frac{2\gamma}{\gamma-1} \left[ 1 - \left( \frac{p_e}{p_c} \right)^{\frac{\gamma-1}{\gamma}} \right] \right\}^{\frac{1}{\gamma}} + \left( \frac{p_e}{p_c} - \frac{p_a}{p_c} \right) \frac{A_e}{A_t} \quad (2)$$

Rewriting the ideal thrust expression:

$$F = p_c A_t \left\{ \frac{2\gamma^2}{\gamma-1} \left( \frac{2}{\gamma+1} \right)^{\frac{\gamma+1}{2(\gamma-1)}} \left[ 1 - \left( \frac{p_e}{p_c} \right)^{\frac{\gamma-1}{\gamma}} \right]^{\frac{1}{\gamma}} \right\} + (p_e - p_a) A_e \quad (3)$$

it is possible to note that the thrust developed depends only on chamber pressure and does not depend on the particular choice of propellants (except than through  $\gamma$ ).

This poses a question: production of light species from the cracking is hampered by pressure, while thrust is favoured. Thus, the optimal pressure that satisfies all requirements must be searched.

Figure 15 shows thrust versus pressure ratio (between nozzle inlet and outlet) at  $P_{\text{combustion}}=1\text{atm}$ ,  $\Phi=1$  and assuming a throat diameter of  $100\mu\text{m}$ . The corresponding expansion ratios are also plotted.

It must be noted that viscous effects are not considered, though they are not negligible for these applications. For example, at  $P_{\text{combustion}}=10\text{atm}$ , the corresponding Reynolds number is:

$$\text{Re} = \frac{\rho u D}{\mu} = \frac{5 \times 10^{-1} \times 1000 \times 100 \times 10^{-6}}{10^{-4}} = 500$$

Even though the viscous effects have not such substantial influence, they should be taken in account through a losses factor in order to decrease performance compared to the ideal case. Furthermore, as the pressure decreases, the Reynolds number decreases as well, thus viscous effects rise.

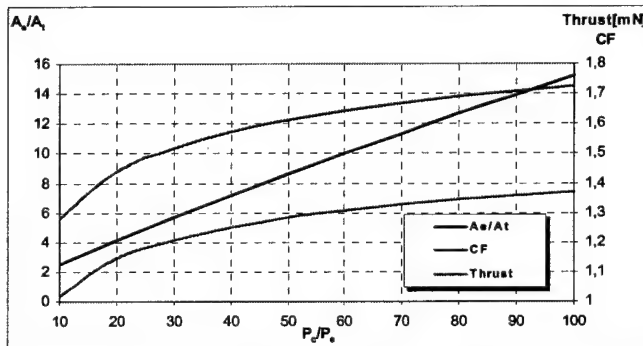


Figure 15  $P_{\text{combustion}}=1\text{atm}$ ,  $T_{\text{combustion}}=905.17\text{K}$ ,  $\Phi=1$

This figure shows that as the pressure ratio increases, the thrust developed increases as well, going from  $1\text{mN}$  assuming a pressure ratio of 10, to  $1.37\text{mN}$  at pressure ratio of 100. At the same time the expansion ratio goes from 2 to 15. The expansion ratio influence on performance is explored in figures 16-19. These are obtained at the same previous pressure and temperature conditions, but assuming two different expansion ratio: 50 and 100 (see table 2).

CRACKING	COMBUSTION
$T_{\text{cracking}}^{(1)} = 1000\text{K}$	$T_{\text{combustion}}^{(2)} = 905.17\text{K}$
$T_{\text{cracking}}^{(2)} = 905.17\text{K}$	$P_{\text{combustion}} = 1\text{atm}$
$P_{\text{cracking}} = 1\text{atm}$	$A_e/A_t = 50-100$

Table 2

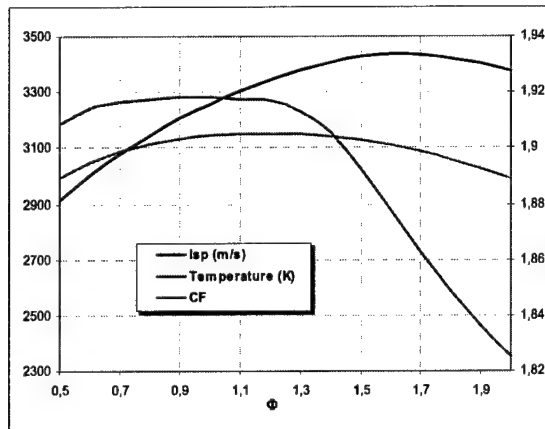


Figure 16  $P_{\text{combustion}}=1\text{atm}$ ,  $T_{\text{combustion}}=905.17\text{K}$ ,  $\text{Ae/At}=50$

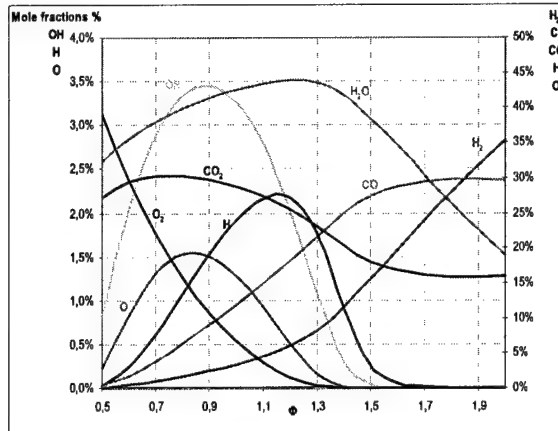


Figure 17  $P_{\text{combustion}}=1\text{atm}$ ,  $T_{\text{combustion}}=905.17\text{K}$ ,  $\text{Ae/At}=50$

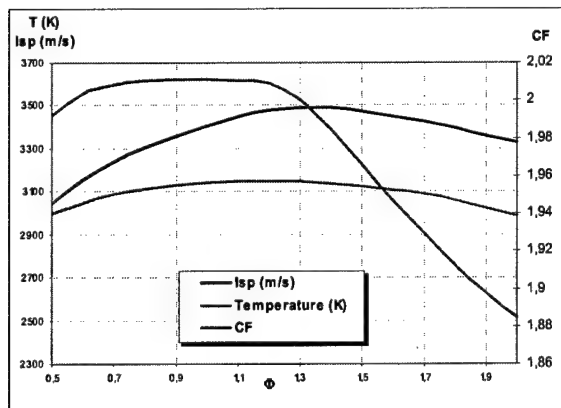


Figure 18  $P_{\text{combustion}}=1\text{atm}$ ,  $T_{\text{combustion}}=905.17\text{K}$ ,  $\text{Ae/At}=100$

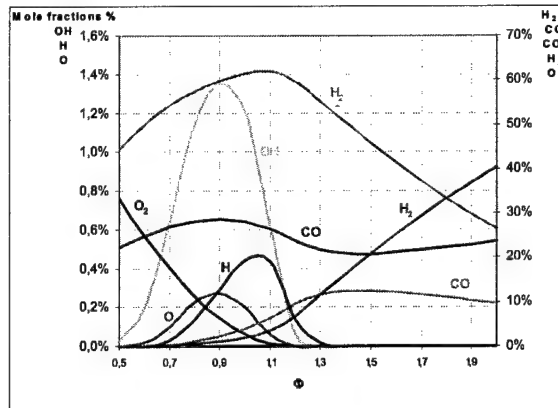


Figure 19  $P_{\text{combustion}}=1\text{atm}$ ,  $T_{\text{combustion}}=905.17\text{K}$ ,  $\text{Ae/At}=100$

The comparison between the different thrust coefficient and specific impulse, at the different equivalence ratios, and expansion ratios is reported in figures 20-21.

These figures show that as the expansion ratio increases, the specific impulse increases as well, due to the higher pressure ratio. As the expansion ratio increases, optimal performance is obtained at smaller equivalence ratios: from  $Isp=3420\text{m/s}$  and  $\Phi=1.6$  at  $\text{Ae/At}=100$  to  $Isp=2990\text{m/s}$  and  $\Phi=1.8$  at  $\text{Ae/At}=10$ . Correspondently, the thrust coefficient increases going from 1.64 to 2 by about 18%, suggesting higher and higher expansion ratios, but the requisite of size as small as possible may establish an upper limit, depending on application.

Since the combustion pressure must be lower than cracking pressure, at  $P_{\text{cracking}}=1\text{atm}$  only  $P_{\text{combustion}}=1\text{atm}$  is examined.

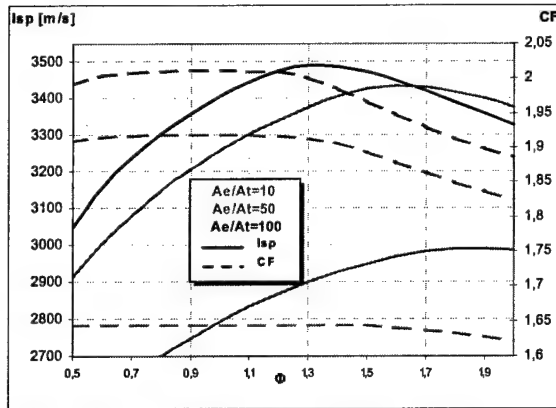


Figure 20  $P_{\text{combustion}}=1\text{atm}$ ,  $T_{\text{combustion}}=905.17\text{K}$ ,  $Ae/\text{At}=10, 50, 100$

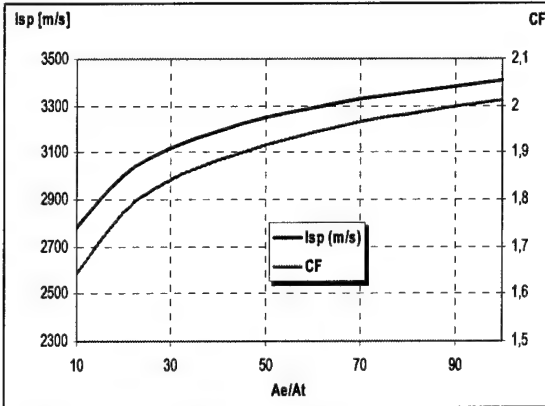


Figure 21  $P_{\text{combustion}}=1\text{atm}$ ,  $T_{\text{combustion}}=905.17\text{K}$ ,  $\Phi=1$

The figures below, show results obtained varying the cracking pressure ( $P_{\text{cracking}}=5\text{atm}$ ), and, as a consequence, the products of cracking and their initial combustion temperature. The initial conditions are reported in table 3:

CRACKING	COMBUSTION
$T_{\text{cracking}}^{(1)}=1000\text{K}$	$T_{\text{combustion}}^{(2)}=986.62\text{K}$
$T_{\text{cracking}}^{(2)}=986.62\text{K}$	$P_{\text{combustion}}=1\text{atm}$
$P_{\text{cracking}}=5\text{atm}$	$Ae/\text{At}=10$

Table 3

The comparison between figures 22-23 and 12-13, plotted also in figure 26, shows that (unlike by the effect of chamber pressure), increasing the cracking pressure, the specific impulse decreases. The maximum specific impulse goes from 3050m/s at  $P=1\text{atm}$  to 2900m/s at  $P=5\text{atm}$ . This effect is due to the heavier cracking products produced at higher pressure (as pointed out in the previous section) and lower combustion chamber temperature (see fig. 23 and 12). At the same time, CF increases with cracking pressure only above  $\Phi=1.6$ .

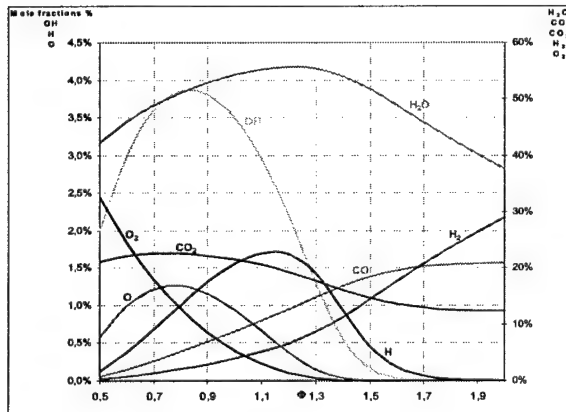


Figure 22  $P_{\text{combustion}}=1\text{atm}$ ,  $T_{\text{combustion}}=986.62\text{K}$ ,  $Ae/\text{At}=10$

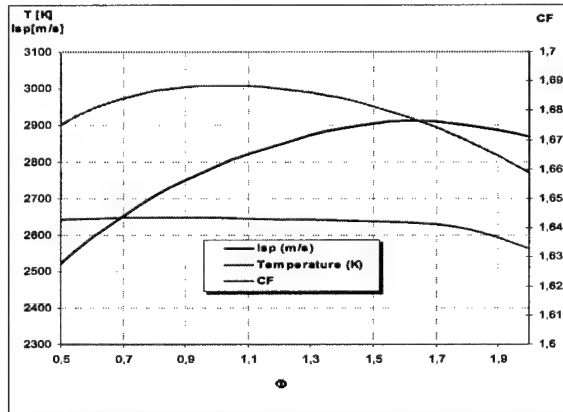


Figure 23  $P_{\text{combustion}}=1\text{atm}$ ,  $T_{\text{combustion}}=986.62\text{K}$ ,  $Ae/\text{At}=10$

Figures 24-25 show the performance at the following conditions:

CRACKING	COMBUSTION
$T_{cracking}^{(1)} = 1000K$	$T_{combustion}^{(2)} = 986.62K$
$T_{cracking}^{(2)} = 986.62K$	$P_{combustion} = 5atm$
$P_{cracking} = 5atm$	$Ae/At = 10$

Table 4

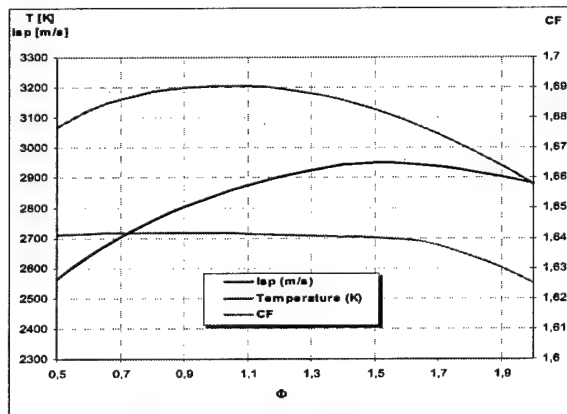


Figure 24  $P_{combustion}=5atm$ ,  $T_{combustion}=986.62K$ ,  $Ae/At=10$

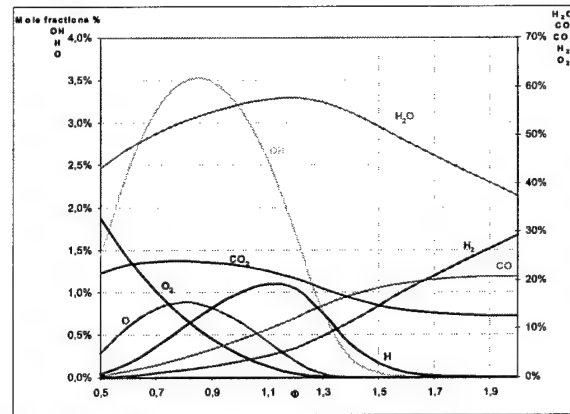


Figure 25  $P_{combustion}=5atm$ ,  $T_{combustion}=986.62K$ ,  $Ae/At=10$

In order to analyse the combustor and cracking pressure influence on the specific impulse and thrust coefficient, these are plotted together in figures 26-27.

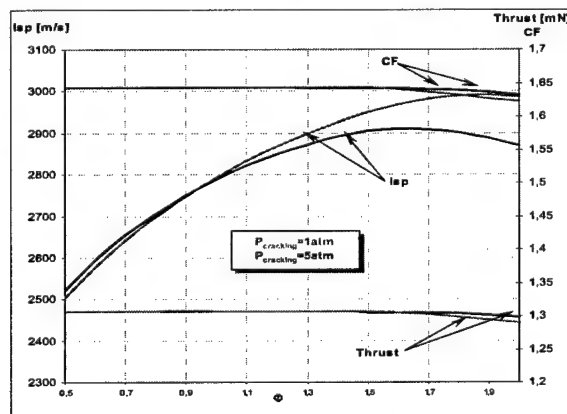


Figure 26  $P_{combustion}=5 atm$ ,  $P_{cracking}=1,5 atm$ ,  $Ae/At=10$

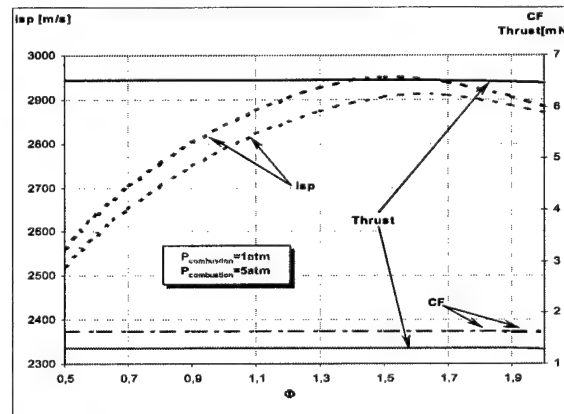


Figure 27  $P_{combustion}=1,5 atm$ ,  $P_{cracking}= 5 atm$ ,  $Ae/At=10$

Figure 26 points out that as cracking pressure increases, the specific impulse decreases, while the thrust and the thrust coefficient increase negligibly. As a preliminary evaluation, lower cracking pressures improve microrockets performance. However, the cracking pressure must

be higher than combustion pressure, therefore an estimate of combustion pressure influence on performance is evaluated in figure 27.

Increasing combustor pressure has a positive effect on specific impulse. In order to increases the specific impulse by about 40m/s (going from 2910m/s at  $P_{C.C.}=1\text{atm}$ , to 2950m/s at  $P_{C.C.}=5\text{atm}$ ) the equivalence ratio must decrease from  $\Phi=1.6$  to  $\Phi=1.5$ .

Besides, figure 27 points out that the combustion pressure has a favourable role on thrust: in fact, it lets thrust reach higher and higher values. Furthermore, as pressure increases, the engine size becomes smaller.

Figures 28-31 show specific impulse, temperature and mole fractions for combustor chamber pressure  $P=5\text{atm}$  and at  $Ae/At=50$  and 100. Table 5 reports the initial conditions:

CRACKING	COMBUSTION
$T_{\text{cracking}}^{(1)} = 1000\text{K}$	$T_{\text{combustion}}^{(2)} = 986.62\text{K}$
$T_{\text{cracking}}^{(2)} = 986.62\text{K}$	$P_{\text{combustion}} = 5\text{atm}$
$P_{\text{cracking}} = 5\text{atm}$	$Ae/At = 50, 100$

Table 5

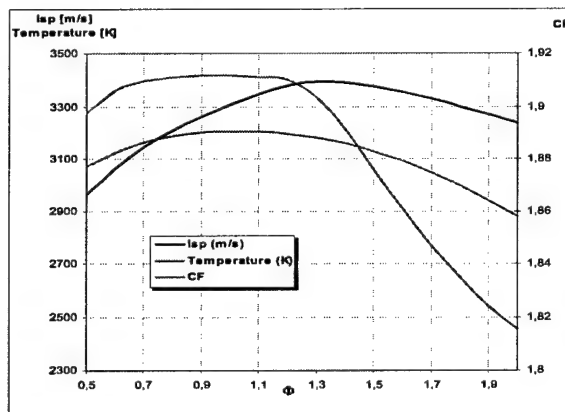


Figure 28  $P_{\text{combustion}}=5\text{atm}$ ,  $T_{\text{combustion}}=986.62\text{K}$ ,  $Ae/At=50$

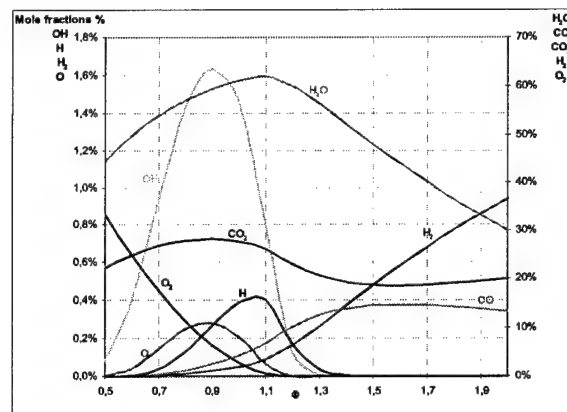


Figure 29  $P_{\text{combustion}}=5\text{atm}$ ,  $T_{\text{combustion}}=986.62\text{K}$ ,  $Ae/At=50$

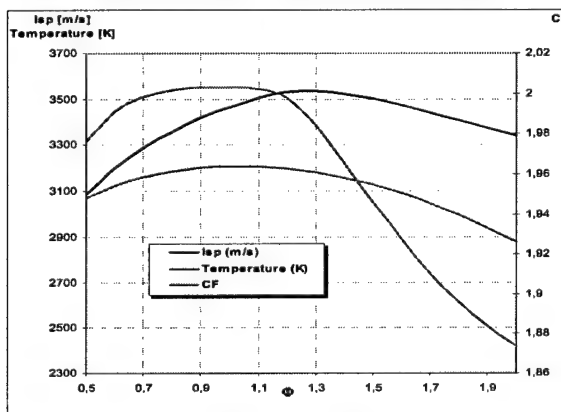


Figure 30  $P_{\text{combustion}}=5\text{atm}$ ,  $T_{\text{combustion}}=986.62\text{K}$ ,  $Ae/At=100$

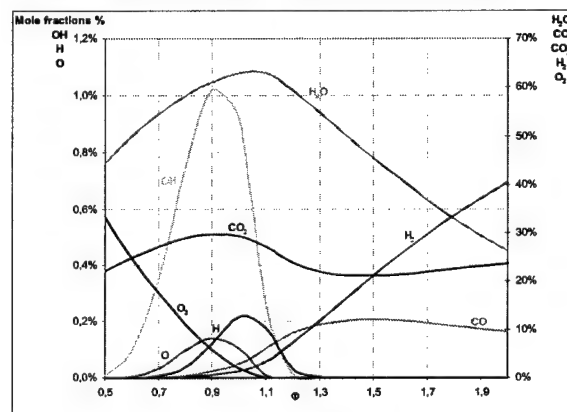


Figure 31  $P_{\text{combustion}}=5\text{atm}$ ,  $T_{\text{combustion}}=986.62\text{K}$ ,  $Ae/At=100$

Figure 32 points out the positive effect of the expansion ratio increase (at  $P_{\text{combustion}}=5\text{atm}$ ) on the specific impulse and the thrust coefficient.

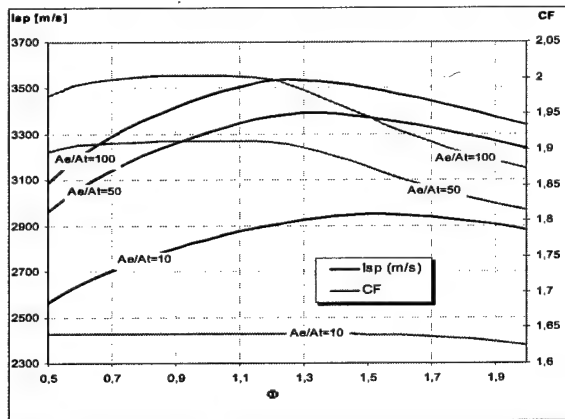


Figure 32  $P_{\text{combustion}}=5\text{atm}$ ,  $T_{\text{combustion}}=986.62\text{K}$ ,  $Ae/At=10, 50, 100$

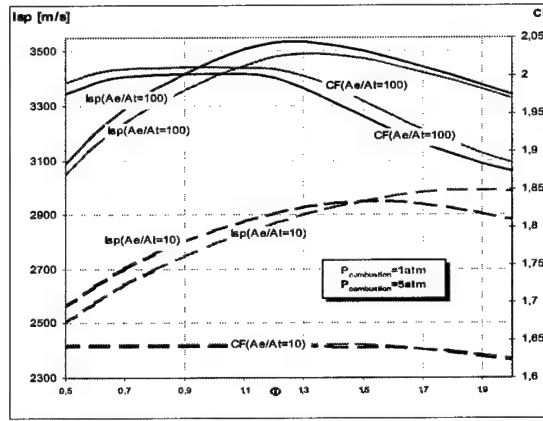


Figure 33  $P_{\text{combustion}}=1, 5\text{atm}$ ,  $T_{\text{combustion}}=986.62\text{K}$ ,  $Ae/At=10, 100$

Figure 33 shows that raising chamber pressure raises also the specific impulse and thrust, but this also depends on expansion ratio. In fact, assuming  $Ae/At=100$ , at  $P_{\text{combustion}}=5\text{atm}$ , the specific impulse is always higher than that calculated at  $P_{\text{combustion}}=1\text{atm}$ ; while assuming  $Ae/At=10$ , this is not always true. The explanation is found in the competition between combustion temperature and the average molecular weight, that increase both with pressure. Figures 34-39 show the engine performance at the following conditions:

CRACKING	COMBUSTION
$T_{\text{cracking}}^{(1)}=1000\text{K}$	$T_{\text{combustion}}^{(2)}=1204\text{K}$
$T_{\text{cracking}}^{(2)}=1204\text{K}$	$P_{\text{combustion}}=1, 5, 10\text{atm}$
$P_{\text{cracking}}=10\text{atm}$	$Ae/At=10$

Table 6

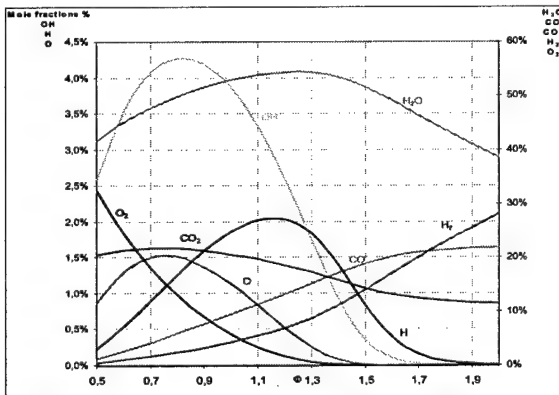


Figure 34  $P_{\text{combustion}}=1\text{atm}$ ,  $T_{\text{combustion}}=1204\text{K}$ ,  $Ae/At=10$

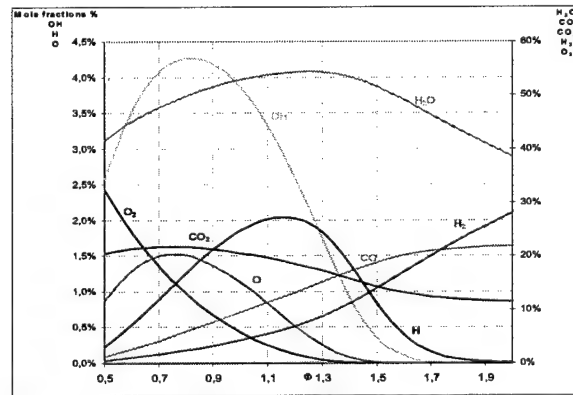


Figure 35  $P_{\text{combustion}}=1\text{atm}$ ,  $T_{\text{combustion}}=1204\text{K}$ ,  $Ae/At=10$

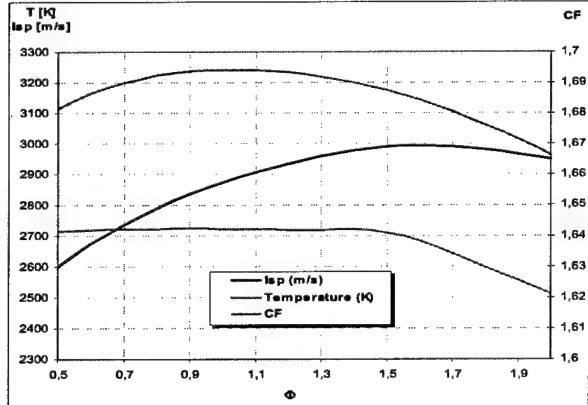


Figure 36  $P_{\text{combustion}}=5\text{atm}$ ,  $T_{\text{combustion}}=1204\text{K}$ ,  $\text{Ae}/\text{At}=10$

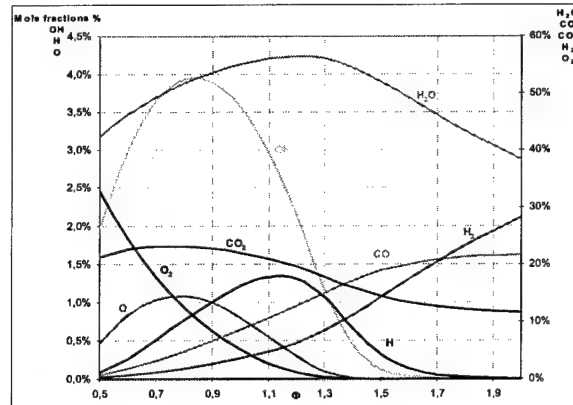


Figure 37  $P_{\text{combustion}}=5\text{atm}$ ,  $T_{\text{combustion}}=1204\text{K}$ ,  $\text{Ae}/\text{At}=10$

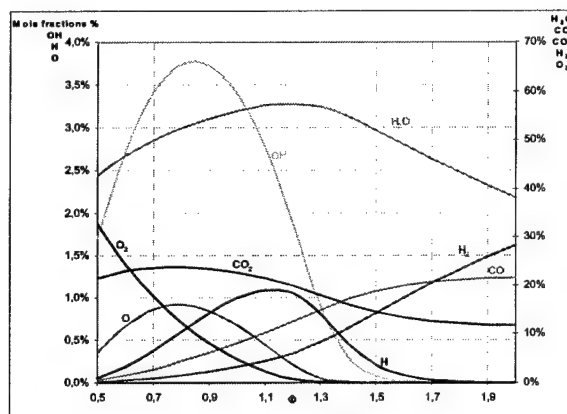


Figure 38  $P_{\text{combustion}}=10\text{atm}$ ,  $T_{\text{combustion}}=1204\text{K}$ ,  $\text{Ae}/\text{At}=10$

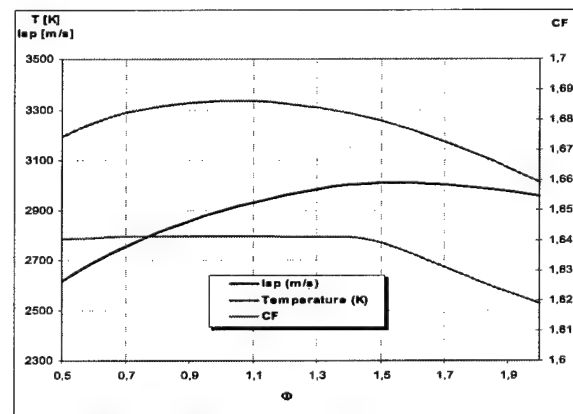


Figure 39  $P_{\text{combustion}}=10\text{atm}$ ,  $T_{\text{combustion}}=1204\text{K}$ ,  $\text{Ae}/\text{At}=10$

Figure 40-44 show the results obtained at the initial condition reported in table 7:

CRACKING	COMBUSTION
$T_{\text{cracking}}^{(1)} = 1000\text{K}$	$T_{\text{combustion}}^{(2)} = 1204\text{K}$
$T_{\text{cracking}}^{(2)} = 1204\text{K}$	$P_{\text{combustion}} = 10\text{atm}$
$P_{\text{cracking}} = 10\text{atm}$	$\text{Ae}/\text{At} = 50,100$

Table 7

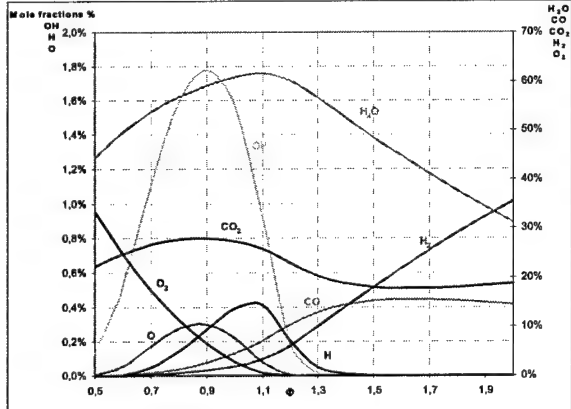


Figure 40  $P_{\text{combustion}}=10\text{atm}$ ,  $T_{\text{combustion}}=1204\text{K}$ ,  $\text{Ae}/\text{At}=50$

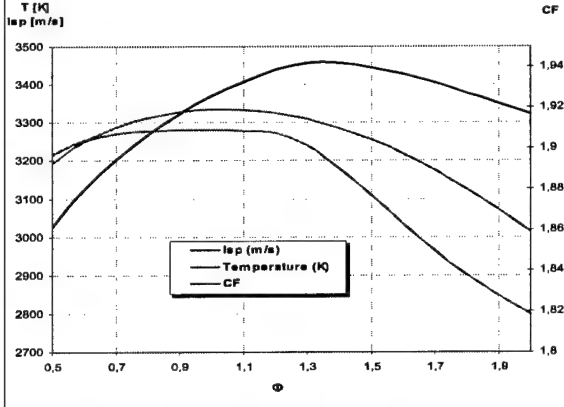


Figure 41  $P_{\text{combustion}}=10\text{atm}$ ,  $T_{\text{combustion}}=1204\text{K}$ ,  $\text{Ae}/\text{At}=50$

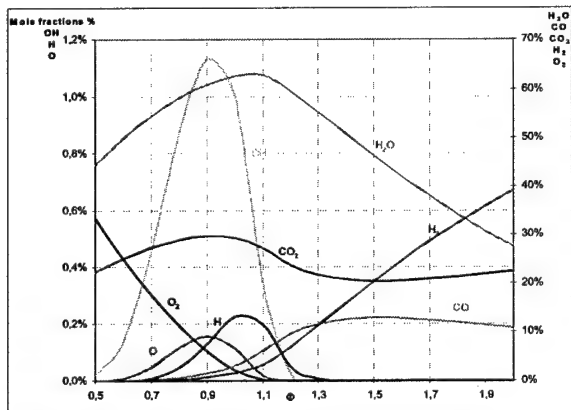


Figure 42  $P_{\text{combustion}}=10\text{atm}$ ,  $T_{\text{combustion}}=1204\text{K}$ ,  $\text{Ae}/\text{At}=100$

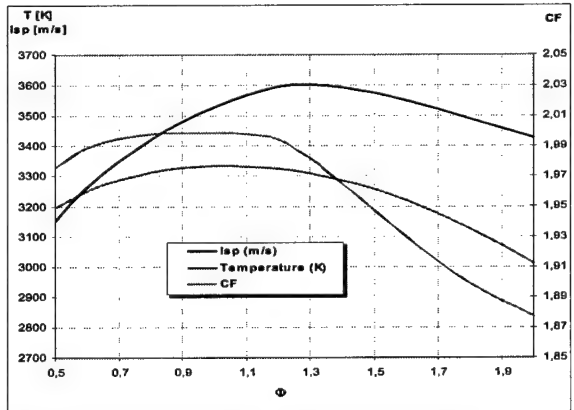


Figure 43  $P_{\text{combustion}}=10\text{atm}$ ,  $T_{\text{combustion}}=1204\text{K}$ ,  $\text{Ae}/\text{At}=100$

Figures 44-46 show the expansion ratio and combustion pressure influence on the specific impulse and the thrust coefficient at  $P_{\text{cracking}}=10\text{atm}$ .

Figure 45 shows that the combustion pressure influences engine performance. It points out that as pressure increases, the specific impulse increases as the combustion chamber temperature. The thrust coefficient decreases a little, but figure 47 shows that the thrust increases.

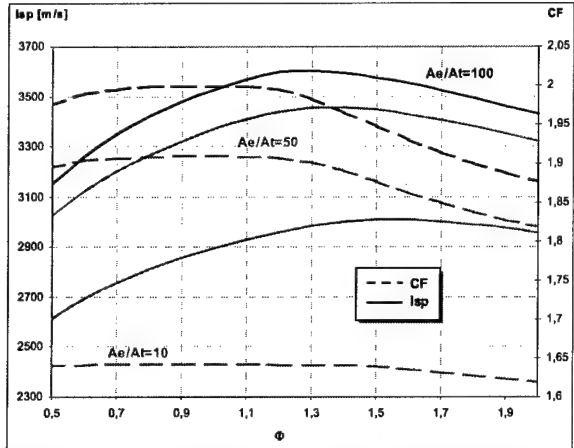


Figure 44  $P_{\text{combustion}}=10\text{ atm}$ ,  $T_{\text{combustion}}=1204\text{ K}$ ,  $Ae/At=10, 50, 100$

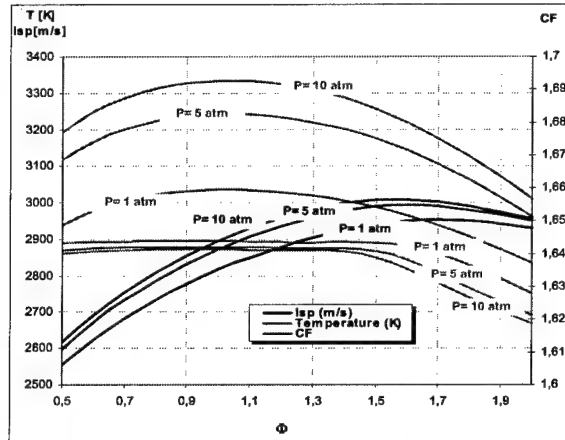


Figure 45  $P_{\text{combustion}}=1, 5, 10\text{ atm}$ ,  $P_{\text{cracking}}=10\text{ atm}$ ,  $Ae/At=10$

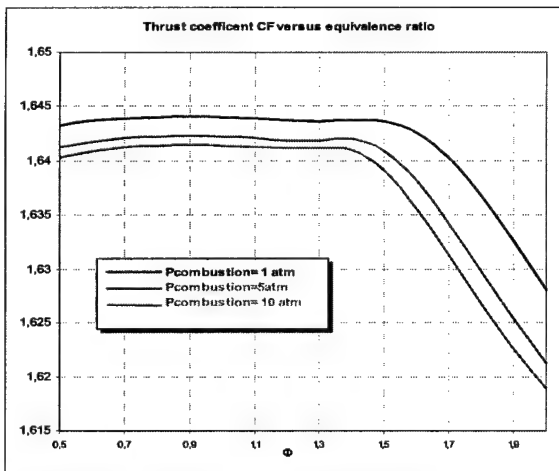


Figure 46  $P_{\text{crack}}=10\text{ atm}$ ,  $T_{\text{combustion}}=1204\text{ K}$ ,  $Ae/At=10$

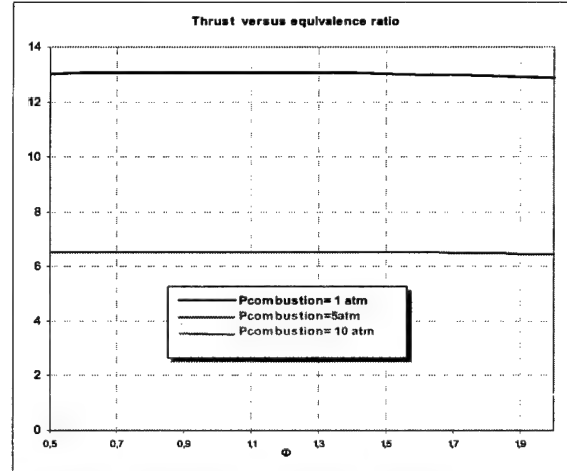


Figure 47  $P_{\text{crack}}=10\text{ atm}$ ,  $T_{\text{combustion}}=1204\text{ K}$ ,  $Ae/At=10$

Figures 48-50 show the combined influence of cracking and combustion pressure on CF, thrust and Isp.

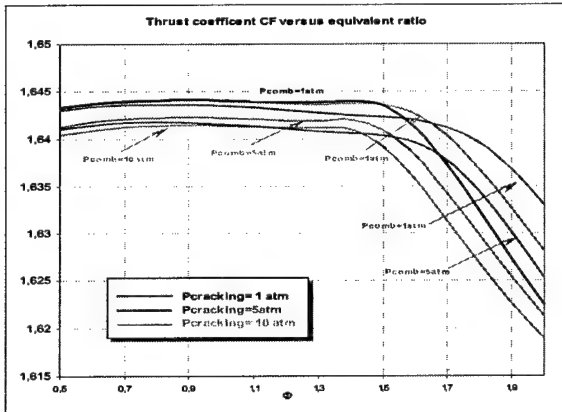


Figure 48  $Ae/At=10$

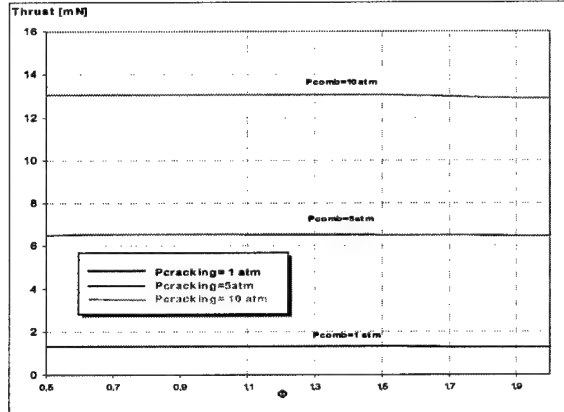


Figure 49  $Ae/At=10$

These figures point out that the cracking pressure has a weak influence on CF, and, therefore, its influence on thrust is negligible. The effect of cracking pressure on specific impulse is to reduce  $Isp$  substantially. At the same time, the specific impulse increases with chamber pressure. Therefore, pressure affects performance in opposite ways. This raises a question: since the cracking pressure must be higher than chamber pressure, what is the better choice, to lower cracking pressure or to raise chamber pressure and therefore cracking pressure? Figure 49 shows that in order to have high thrust, pressure should be raised. Figure 50 shows that increasing the chamber pressure, the positive effects on specific impulse overcome the negative effects of the cracking pressure. Thus, in order to maximize both the specific impulse and thrust, high pressures must be used.

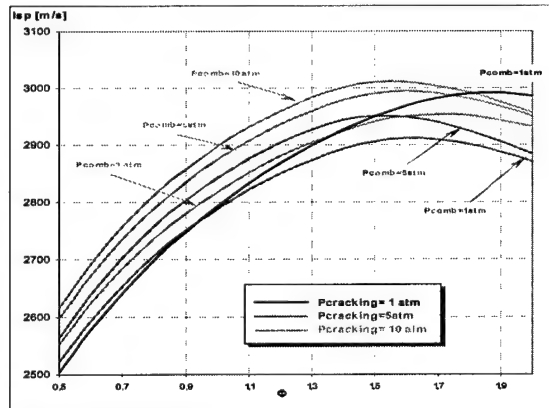


Figure 50  $Ae/At=10$

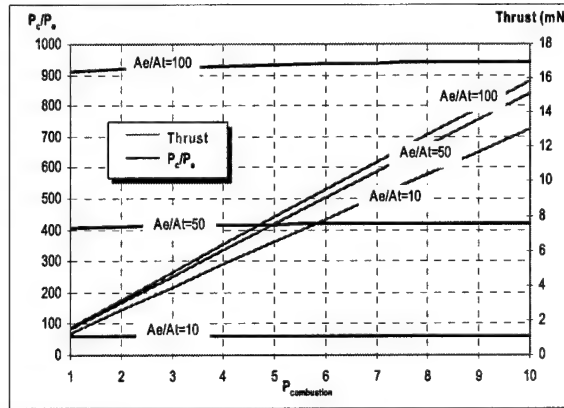


Figure 51 ( $\Phi=1$ )

Figure 51 shows thrust and pressure ratio versus combustion chamber pressure ( $\Phi=1$ ). Assuming  $Ae/At=10$ , it shows thrust going from 1.3mN to 13mN respectively changing  $P_c$  from 1atm and to 10atm. Besides, increasing the expansion ratio until 100, the thrust reaches 16mN.

## 4 Conclusions

In this Part, we analysed the equilibrium products of methyl alcohol cracking. The results are:

1. thanks to its low specific volume, methyl alcohol allows the use of compact tanks;
2. the cracking process enables production of onboard hydrogen and other combustible species;
3. methanol dissociates mainly into molecular hydrogen (45%), but also into methane, water, dioxide carbon and monoxide carbon and graphite;
4. as cracking pressure increases, light species decrease;
5. above a threshold temperature (which depends on pressure), the cracking mechanism becomes endothermic and the heat necessary to enable cracking reactions can be supplied by the combustor walls.

We also examined the ideal rocket performance obtained burning cracking products and oxygen. Our conclusions are:

1. As the cracking pressure increases, the specific impulse decreases. Since the cracking products must be injected within the combustion chamber, the cracking process must be performed at pressure higher than the combustor pressure.
2. Increasing combustion pressure raises thrust and specific impulse; in addition, reduces ignition delay time, via speeding up kinetics reactions.
3. In order to maximize thrust, higher nozzle expansion ratios should be used.
4. Specific impulse of order 2500-3000 m/s and thrust of 1.5-16 mN can be reached.

In Part 1 we performed a simplified analysis of inlet temperature  $T_i$  on chamber temperature  $T_g$ . Higher  $T_i$  corresponds to the case of reformed reactants as fuel. Increasing  $T_i$  implies to increase the chamber temperature  $T_g$ .

## Part III

# Catalytic Combustion Enhancement

### 1 Introduction

We have seen that quenching limits (pag. 9) due to *HT* pose limits to miniaturizing *LRE*, even when using regenerative reforming of the primary fuel. Synthesizing much information, quenching is ruled mostly by characteristic times: that of the heat-releasing kinetics between propellants, and that of *HT* (losses) to walls, or to colder gas (flame stretching) if flow is turbulent.

There is little hope to reduce losses beyond what already suggested in previous analyses; so, the question is whether kinetics could be made faster. In fact, using heterogeneous catalysts the answer to this question is affirmative: the overall effect of catalysis is akin to lowering the gas-phase activation energy. A catalyst does not change final (equilibrium) composition of products, merely speeds up the kinetics leading to equilibrium. Physically, an heterogeneous catalyst may be seen as a place where reacting species are adsorbed (typically, with a negative  $\Delta G$ ,  $G$  being the Gibbs energy), and can react either between themselves or with gas-phase reactants. For instance,  $H_2$  (gas) may react with  $OH$  radicals adsorbed on Group VIII metals (such as *Pt* or *Pd*) forming water; in automotive catalysts, one of the main mechanisms for *CO* oxidation is due to collisions between passing  $O_2$  molecules and *CO* adsorbed. In the first case the distance between reactants is of order of the lattice size, i.e., at least an order of magnitude lower than in the gas phase at *STP*. In the second, the collisional frequency is higher. Whatever the physical interpretation for the catalytic processes, they are faster than equivalent gas-phase mechanisms.

What this means in practice is that combustion kinetics in the presence of an appropriate catalyst will be fast, and may be faster than heat transfer. If the catalyst is deposited on the very walls of the miniature *LRE*, reactions may occur right on the walls and be completed while part of the heat release is transferred to the wall. In the limit, gas phase kinetics becomes immaterial, most of the chemistry occurring at the surface. Thus quenching due to cooler walls may be overcome by the very fact that kinetics occurs at the walls. While this occurs, the walls may be hotter than if no catalysis was present, a positive consequence for propellant kinetics, in that it speeds it up. Shrinking more and more the *LRE* eventually even catalysis cannot prevent quenching: this will occur when even the rate of catalytic heat release cannot keep up with the rate of heat transfer through the wall. Catalysis may retard quenching, but cannot suppress it altogether.

In this context a catalytic surface will be simply a way to produce enough heat to sustain combustion in the gas phase, or (said otherwise), to raise the temperature of the surface enough or reduce the heat loss through that surface.

Studies of the effect of surface catalysis on maintaining stable combustion are in

[33, 34], the first showing the positive effect on ignition inside a small diameter, catalytically coated tube, and the second near a stagnation point. Of course, much effort has been devoted in the past to study catalytic- or catalytically-assisted combustion, especially for gas turbine combustors; however, the physical situation and geometry being quite different, these studies cannot be directly utilized in microLRE.

## 2 Catalysis and Reforming in MicroRockets

As the characteristic engine size  $D$  shrinks, the ratio between surface  $\sim D^2$  and volume  $\sim D^3$  tends to grow, subtracting more and more of the chemical heat release through the combustion chamber walls. Walls become critical regions of the engine, because 1) heat transfer to the wall increases when shrinking the thruster, 2) they must be cooled and 3) they can quench combustion.

As mentioned in the section about thruster scaling, endothermic reforming of the primary fuel, or propellant, could be a strategy to solve, at least in part, the three problems listed above. Reforming of Liquid Hydrocarbon Fuels (*LHC*) produces  $H_2$ ,  $CO$  and other *HC* species (it may also produce soot). Reforming is endothermic, but reforming products are hotter than the primary *LHC* raising the inlet temperature  $T_i$  of the reforming products injected into the chamber. This also can partly compensate for the reduction of thrust  $F$ , see (9). An additional benefit may possibly accrue by using dense, storable *LHC* as fuel.

Using a catalyst deposited on the chamber inner walls helps in reducing flame quenching and walls thermal loads (heat flux to the walls), because the temperature  $T_{wg}$  at the wall on the gas side rises. Combination of this strategy with reforming will be analyzed in what follows.

The effect of a catalyst will be understood (and then modeled) in a simpler way by picturing its workings along a cross section of the microLRE. From the centerline of the engine outwards, hot gas consisting of reactants and hot products moves to the LRE wall coated with an oxidation catalyst. This motion will be the results of turbulent convection and molecular diffusion. At the wall the catalyst will favor the oxidation of the fuel with the oxidizer, raising the wall surface temperature. Therefore, the heat transfer to the surface from the hot chamber will be accordingly reduced. Across the wall heat will be transferred by thermal conductivity to the primary fuel on the other side (e.g., methanol, or a hydrocarbon). For simplicity, it can be assumed that the heat transferred is spread to the bulk of the primary fuel in a time shorter than the fuel residence time; this is realistic if the residence time of the primary fuel to be reformed,  $L/U_r$ , is longer than the conduction time from the hot wall to the fuel,  $(t_r/2)^2/\alpha$ , where  $t_r$  is the thickness of the cooling/reforming jacket where the primary fuel circulates and is supposed to be reformed or pyrolyzed, and  $\alpha$  is the thermodiffusivity of the primary fuel. Under this simplifying assumption the primary fuel heats and decomposes endothermically to form the secondary products (e.g.,  $CO$ ,  $C_2H_2$ , hydrogen) that will be injected inside the combustor.

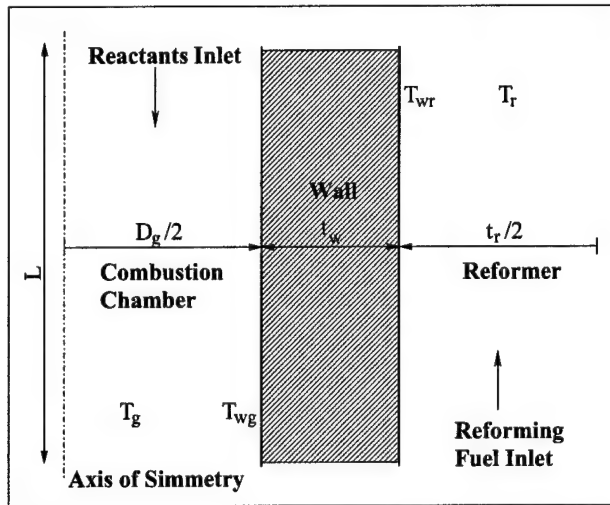


Figure 1: Sketch of the axisymmetric combustion chamber coupled with the coaxial reformer.

Following this conceptual scheme, we consider a combustion chamber sketched in Fig. 32:  $D_g$  (diameter) is its internal characteristic dimension;  $t_w$  is the thickness of the chamber wall; LHC to be reformed coflows in a channel whose characteristic radial dimension is  $t_r$ ;  $L$  is the axial length of the device. In the following the indexes  $g$  and  $r$  are associated to quantities inside the combustion chamber and the reforming channel, respectively. Therefore the indexes  $wg$  and  $wr$  are associated to quantities at the wall on the chamber, and on the reforming side. An approximate, algebraic solution is given below: it shows the positive effect of using a catalytic combustor wall.

The 1-D Energy balance at the combustion chamber / internal wall interface, where catalytic reactions happen, is written as:

$$-\frac{k_w (T_{wr} - T_{wg})}{t_w} - h_g (T_g - T_{wg}) + \dot{q}_{rad,g} = \dot{Q}_{cat} \quad (1)$$

where  $k_w$  is the wall thermal conductivity,  $h_g$  is the heat transfer, or adduction, coefficient,  $\dot{q}_{rad,g}$  is the radiative heat loss from the wall and  $\dot{Q}_{cat}$  is the heat released by catalytic reactions at the wall.

The energy balance at the reforming channel / wall interface is written as:

$$-h_r (T_r - T_{wr}) - \frac{k_w (T_{wg} - T_{wr})}{t_w} = 0 \quad (2)$$

From Eqns. (1) and (2) we can write the wall temperatures  $T_{wg}$  and  $T_{wr}$  as function of  $T_g$  and  $T_r$ :

$$T_{wg} = \frac{T_r + T_g (h_g C_w - 1)}{h_g C_w} + (\dot{Q}_{cat} - \dot{q}_{rad,g}) \frac{h_g C_w - 1}{h_g^2 C_w} \quad (3)$$

and

$$T_{wr} = \frac{T_g + T_r (h_r C_w - 1)}{h_r C_w} + (\dot{Q}_{cat} - \dot{q}_{rad,g}) \frac{1}{h_g h_r C_w} \quad (4)$$

where  $C_w$  is the total transmission coefficient of the wall

$$C_w = \frac{1}{h_g} + \frac{t_w}{k_w} + \frac{1}{h_r} \quad (5)$$

We note that  $(h_g C_w - 1) / h_g^2 C_w$  and  $1 / (h_g h_r C_w)$  are always positive, and therefore  $T_{wg}$  and  $T_{wr}$  rise due to catalysis. This implies that the wall heat transfer from the combustion chamber decreases, and the heat transferred from the wall itself to the reforming fuel increases. In fact, in the scaling analysis of Part 1 (p. 3) we showed that the flux  $W_{TRANS} / D^2$  to the wall increases with decreasing  $D$ :

$$\frac{W_{TRANS}}{D_g^2} \sim A_3 \frac{T_g - T_{wg}}{D_g^{1/2}} \quad (6)$$

Thus shrinking the size of the thruster results in higher and higher thermal loads on the chamber walls. Catalysis reduces the heat flux because  $T_{wg}$  increases.

Now we consider explicitly combustion and reforming. The global, energy balance inside the combustion chamber is written as:

$$\rho_g U_g A_g C_{p_g} T_g - \rho_g^o U_g^o A_g C_{p_g}^o T_g^o + h_g (T_g - T_{wg}) A_{wg} = \dot{Q}_g \quad (7)$$

where  $\dot{Q}_g = \rho_g^o U_g^o A_g \Delta H_{R_g}$  is the heat release rate due to combustion and the superscript  $o$  is associated to inlet quantities into the combustion chamber.  $A_g$  is the cross-section area of the combustion chamber;  $A_{wg}$  is the surface where catalysis happens.  $\Delta H_{R_g}$  is the heat of reaction due to combustion. Assuming constant section we have  $\rho_g^o U_g^o = \rho_g U_g$ .

The energy balance in the reforming channel or jacket surrounding the chamber is written as:

$$\rho_r U_r A_r C_{p_r} T_r - \rho_r^o U_r^o A_r C_{p_r}^o T_r^o - h_r (T_{wr} - T_r) A_{wr} = \dot{Q}_r \quad (8)$$

where  $\dot{Q}_r = \rho_r^o U_r^o A_r \Delta H_{R_r}$  is the heat release rate due to reforming, and the superscript  $o$  is associated to inlet quantities into the reforming channel.  $A_r$  is the cross-section area of the reformer;  $A_{wr}$  is the surface transferring heat to the fuel to be reformed.  $\Delta H_{R_r}$  is the heat of reaction due to reforming. Assuming constant section we have  $\rho_r^o U_r^o = \rho_r U_r$ .

Solving equations from (1) to (8), estimating the heat transfer coefficients as:

$$h = \frac{k N u}{L} = \frac{k}{L} P r^a R e^b \quad (9)$$

areas as

$$A_g = \pi (D_g / 2)^2 \quad (10)$$

$$A_{wg} = \pi D_g L \quad (11)$$

$$A_r = \pi \left[ (D_g/2 + t_w + t_r)^2 - (D_g/2 + t_w)^2 \right] \quad (12)$$

$$A_{wr} = 2\pi (D_g/2 + t_w) L \quad (13)$$

and considering that in a microrocket  $L \approx D$ , we obtain the catalytic wall temperature

$$\begin{aligned} T_{wg} = & \frac{\xi}{k_g Pr_g^a Re_g^b \varphi} \left[ (\dot{Q}_{cat} - \dot{q}_{rad,g}) D_g Pr_g^{-a} Re_g^{-b} \psi + \frac{4}{\pi} \frac{\dot{Q}_g}{D_g} + C_{p_g}^o T_g^o \mu_g Re_g \right] + \\ & + \frac{\psi}{\pi k_g Pr_g^a Re_g^b \varphi} \left[ \frac{\dot{Q}_r}{D_g} + \pi C_{p_r}^o T_r^o \mu_r Re_r \left( 1 + 2 \frac{t_w}{D_g} + \frac{t_r}{D_g} \right) \right] \end{aligned} \quad (14)$$

where

$$\varphi = Pr_g Re_g \left( 1 + 2 \frac{t_w}{D_g} \right) + k_r Pr_r Re_r \left( 1 + 2 \frac{t_w}{D_g} + \frac{t_r}{D_g} \right) \left( \frac{4}{k_g} + \frac{C_w}{D_g} Pr_g Re_g \right) \quad (15)$$

$$\xi = Pr_g^a Re_g^b \left( 1 + 2 \frac{t_w}{D_g} \right) - k_r Pr_r Re_r \left( 1 + 2 \frac{t_w}{D_g} + \frac{t_r}{D_g} \right) \left( \frac{1}{k_g} - \frac{C_w}{D_g} Pr_g^a Re_g^b \right) \quad (16)$$

$$\psi = Pr_g Re_g + 4 Pr_g^a Re_g^b \quad (17)$$

Note that the groups  $\varphi, \xi, \psi$  are nondimensional and that we considered explicitly the ratios  $t_w/D_g$  and  $t_r/D_g$ , that could be assumed constant when shrinking the thruster size.

The heat transfer coefficient of the wall (5) can be written as

$$C_w = D_g \left[ \frac{1}{k_g Pr_g^a Re_g^b} + \frac{t_w/D_g}{k_w} + \frac{1}{k_r Pr_r^a Re_r^b} \right] \quad (18)$$

and the heat release rates can be estimated as explained in the next section.

Equation (14) shows how the catalytic wall temperature scales with some characteristic nondimensional groups that depend on geometry, temperature and composition in a complex way. A parametric analysis of this expression (by means of different plots) would show the relative importance of the variables involved. This analysis is not performed in this Report since it depends on actual numbers, i.e., on thrust, sizes, etc. of actual devices, or families of devices. Rather in the present study we want to focus on how catalysis and reforming can actually help in avoiding quenching, stabilizing combustion and enhancing performance in microrockets.

## 2.1 Scaling of the Catalytic Heat Release

In order to analyze scaling effects on catalytic heat release rate we must make some assumptions. When quenching takes place, the conductive time to the wall is less than the catalytic chemical time. Therefore, when combustion takes place we focus on catalytic chemical time. The total heat released in the combustion chamber  $\dot{Q}_g^{TOT} =$

$\rho_g U_g A_g \Delta H_{R_g}$  is given by  $\dot{Q}_{cat} A_{wg} + \dot{Q}_g$ . Assuming that the catalytic chemical time is shorter than the mass diffusion time to the wall (this is realistic at sufficiently high  $T_{wg}$ ), the catalytic heat release rate can be assumed proportional to the reactants diffusive flow rate to the wall,  $\dot{m}_{wg}$ . Therefore

$$\dot{Q}_g^{TOT} = \rho_g U_g A_g \Delta H_{R_g} \equiv \dot{Q}_{cat} A_{wg} + \dot{Q}_g \quad (19)$$

The catalytic heat release rate can be expressed as

$$\dot{Q}_{cat} = \rho_g V_{diff} A_{wg} \Delta H_{R_g} = \frac{\rho_g D_g/2}{\tau_D} A_{wg} \Delta H_{R_g} = \frac{\rho_g D_{mix,g}}{D_g/2} A_{wg} \Delta H_{R_g} \quad (20)$$

where  $V_{diff}$  is the diffusion velocity to the wall,  $\tau_D$  is the mass diffusive time to the wall and  $D_{mix,g}$  is the mass diffusivity. Therefore the heat release rate in the gas can be obtained as difference between that due to catalysis and the total heat release when all propellants are consumed:

$$\dot{Q}_g = \rho_g U_g A_g \Delta H_{R_g} - \dot{Q}_{cat} A_{wg} = \rho_g \left( U_g A_g - \frac{D_{mix,g} A_{wg}}{D_g/2} \right) \Delta H_{R_g} \quad (21)$$

Considering equations (10) and (11) we have

$$\dot{Q}_{cat} = 2\pi \rho_g D_{mix,g} D_g \Delta H_{R_g} \quad (22)$$

and

$$\dot{Q}_g = \pi D_g \left( \frac{\mu_g Re_g}{4} - 2\rho_g D_{mix,g} \right) \Delta H_{R_g} \quad (23)$$

Using then eqn. (12) the heat release rate due to reforming is

$$\dot{Q}_r = \rho_r U_r A_r \Delta H_{R_r} = \pi \mu_r Re_r D_g \left( 1 + \frac{t_w}{2D_g} + \frac{t_r}{D_g} \right) \Delta H_{R_r} \quad (24)$$

### 3 Effects on Thrust and Quenching

On page 4 we showed that the effective thrust  $F$  scales (for an ideal nozzle!) as

$$F \sim A_5 D_g^2 T_g^{1/2} \sim A_5 D_g^2 \left( \frac{A_1 D_g^{3/2} + A_3 T_{wg} + A_4 T_g^o D_g^{1/2}}{A_3 + A_4 D_g^{1/2}} \right)^{1/2} \quad (25)$$

Therefore, the thrust scales with a power  $\sim 5/2$  of the size  $D_g$ . This implies a drastic reduction of thrust as  $D_g$  shrinks. Using catalysis and reforming both  $T_{wg}$  and  $T_g^o$  increase, thus compensating for this effect and raising the thrust. We note that to estimate the scaling of thrust (and of the following performance parameters) with the size  $D_g$  it is necessary to calculate  $T_g^o = T_r$  as previously done for  $T_{wg}$ .

Also the specific impulse is enhanced by using catalysis and cracking, as shown by

$$I_{sp} = \frac{F}{\dot{m}_F} = \frac{F}{\rho_F U_F A_F} = \frac{F}{\rho_r U_r A_r} \quad (26)$$

having considered that the fuel is the reformed gas. Using equations (12) and (25) we have

$$I_{sp} \sim \frac{A_5 D_g}{\pi \mu_r Re_r \left(1 + \frac{t_w}{2D_g} + \frac{t_r}{D_g}\right)} \left( \frac{A_1 D_g^{3/2} + A_3 T_{wg} + A_4 T_g^o D_g^{1/2}}{A_3 + A_4 D_g^{1/2}} \right)^{1/2} \quad (27)$$

In particular, we can see the positive effect of reforming: by using this strategy the thrust scales with a power  $\sim 3/2$  of the size  $D_g$ , and not  $\sim 5/2$  (without considering the scaling of  $T_{wg}$  and  $T_g^o = T_r$  with  $D_g$ ), assuming to shrink the thruster taking constant the ratios  $t_w/D_g$  and  $t_r/D_g$ .

At page 10 we showed that the chemical time,  $t_{ch}$ , for a simple 1-step reaction of order  $n$  scales as

$$t_{ch} \sim A^{-1} \rho_g^{1-n} \exp \left[ \frac{E_a (A_3 + A_4 D_g^{1/2})}{R (A_1 D_g^{3/2} + A_3 T_{wg} + A_4 T_g^o D_g^{1/2})} \right] \quad (28)$$

This time decreases as  $T_{wg}$  and  $T_g^o$  increase due to catalytic and reforming reactions. We also showed that quenching may occur if  $Ka \geq 1$ , i.e., when

$$\frac{1}{KE} \frac{U^3}{D} A^{-1} \rho_g^{1-n} \exp \left[ \frac{E_a (A_3 + A_4 D_g^{1/2})}{R (A_1 D_g^{3/2} + A_3 T_{wg} + A_4 T_g^o D_g^{1/2})} \right] \geq 1 \quad (29)$$

This condition scales with  $D_g$  in a complex way. In fact, for large enough  $D_g$ , stretch may not matter, since  $E_a$  is typically large. However, when  $D_g$  is reduced the gradual reduction of  $T_{wg}$  slows down kinetics until quenching occurs. Thus Expression (29) shows the beneficial effect of reforming, which increases  $T_g^o$  and affects positively (and exponentially) quenching. The same conclusions hold for the effect of catalysis, which also increases  $T_{wg}$ .

## 4 Conclusions

In Part 1 we showed that as the characteristic engine size  $D$  shrinks, the ratio between surface  $\sim D^2$  and volume  $\sim D^3$  tends to grow, subtracting more and more of the chemical heat release through the combustion chamber walls. Walls become critical regions of the engine, because 1) heat transfer to the wall increases when shrinking the thruster, 2) they must be cooled and 3) they can quench combustion. Endothermic reforming of the primary fuel, or propellant, and using a catalyst deposited on

the chamber inner walls could be a strategy to solve, at least in part, these three problems. The analyses presented indicate both strategies can pay off, allowing operation of micro-LRE beyond the conventional limits due to flame quenching and heat losses in general. Further issues that could be investigated are about structural effects and definitely fabrication. The present study can be used as a springboard to preliminary design of micro-LRE (sizing), in conjunction with more detailed, but also more time consuming, CFD calculations.

## Part IV

# Aluminum/Water Operation

## 1 Introduction

In this report, aluminum and water are analyzed to assess their performance potential for microrocket application.

The high heat of combustion of aluminum, its high impulse density, and handling safety are features making it interesting for satellite propulsion, and in particular for compact mini- and micro-rocket engines. The combination aluminum-water **propellants** has been proposed by several authors [Ref.38, 39] for advanced underwater propulsion, where seawater plays the same role of freely available air in airbreathing propulsion.

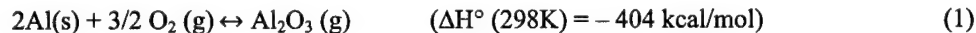
Interest in this combination was also spurred by commercial availability of Al nanoparticles (“ALEX™”) [Ref. 40] and of reports of their successful use in LHC/air combustion. The ratio surface area/mass for nanoparticles is high, ensuring (in principle) fast surface kinetics or fast vaporization once the oxide coating, when present, is cracked. The ‘grain’ or porous sponge combustion with steam of aluminum could be an alternative strategy in conventional rocket hybrid motors. The steam generator would be integral part of the cooling system, i.e., water would be turned into steam by heat transfer from the combustion chamber. Injecting liquid H<sub>2</sub>O into the chamber would require pressurizing its tank, or pumping, i.e., more complexity. Aluminum for space propulsion could also be seen as a “green” propellant.

A remarkable option is to burn pure Aluminum with water bypassing both the heating and melting problems of its oxide.

Since few data on aluminum ignition have been reported, simple or even crude assumptions are employed in what follows.

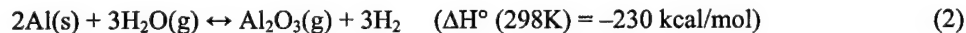
## 2 Aluminum/Water: Theoretical Performance

It is well known that aluminum reacts exothermically with oxygen following the reaction:



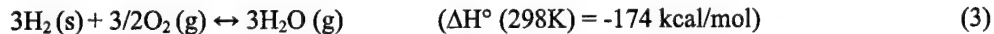
In an oxygen environment an aluminum particle is rapidly coated by a layer of Al<sub>2</sub>O<sub>3</sub>. Several authors suggested Aluminum combustion is heterogeneous: O<sub>2</sub> reacts with the Al<sub>2</sub>O<sub>3</sub> oxide film and diffuses through it to Aluminum surface, where combustion occurs. Thus, in order to ignite Al, it is necessary to raise the surface temperature at least over the Al<sub>2</sub>O<sub>3</sub> melting point (~2327 K): this is part of the so-called “Glassman’s criterion” [Ref. 41]. They stated that a metal burn in the vapour phase if its boiling point temperature was lower than that of its oxide. Ignition delay time, in this case, is controlled by the time needed to heat and melt the Al<sub>2</sub>O<sub>3</sub> layer (so that O<sub>2</sub>, or other oxidant, may diffuse to the Al surface) and the surface kinetics time. For the reason, Friedman and Macek [Ref. 42] assumed Aluminum reactions are negligible at temperature below 2300 K. In order to speed up Aluminum combustion, temperatures higher than that of aluminum vaporization have to be furnished, leading the aluminum and water combustion to take place in gas phase. In fact, once Al vaporizes, kinetics is fast and no longer controls the ignition process.

Lowering the ignition temperatures of Al is in principle possible by oxidizing aluminum with steam, following the reaction:



Gurevich [Ref. 43] found the ignition temperature of (2) to be considerably lower than  $\text{Al}_2\text{O}_3$  melting temperature, but still depending on the crystal structure of the initial oxide film covering the surface of aluminum. Previous work [Ref. 44] has in fact shown that, in a steam atmosphere, aluminum particles are covered by a less protective *hydroxide* layer requiring 'ignition' temperatures to 1600 – 1700 K, and shortening, in turn, ignition time. This option is particularly attractive for underwater propulsion, since the oxidizer is provided directly by the external environment, reducing the on-board oxidizer requirement (but resulting in a lower energy density: i.e. the  $\Delta H^\circ$  for reaction (2) is less than for reaction (1) ).

However, it is possible, in principle, to burn  $\text{H}_2$  produced by (2) with *stored O<sub>2</sub>*:



In other words, following reactions (2) and (3), it is possible to obtain reaction (1) (i.e. the same energy) with less restrictive ignition constraints. Reaction (3) does not need any external ignition source since  $\text{H}_2$  produced in reaction (2) will be above its autoignition temperature with  $\text{O}_2$ . On the other hand, this solution would complicate the whole engine scheme, requiring a tank and pumping. Simplicity and reliability being among the most important micropropulsion requirements, this option was not examined further.

To assess the potential of Al-steam combinations, theoretical performance was evaluated with the NASA's CEA600 *equilibrium* code [Ref. 45].

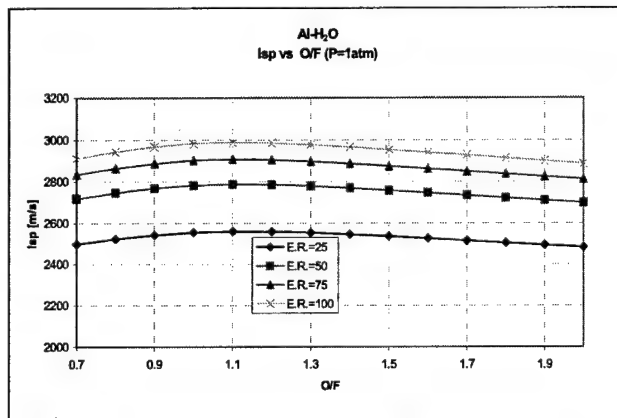


Figure 1: Isp vs O/F for Al-H<sub>2</sub>O system (P=1atm)

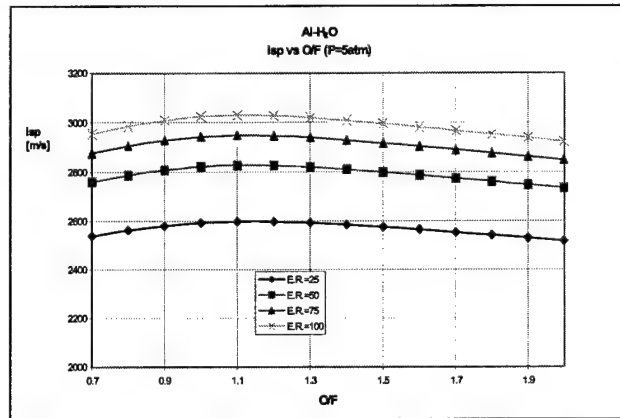


Figure 2: Isp vs O/F for Al-H<sub>2</sub>O system (P=5atm).

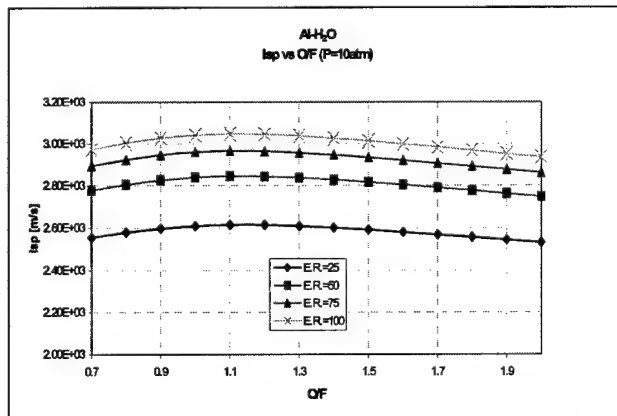


Figure 3: Isp vs O/F for Al-H<sub>2</sub>O system (P=10atm)

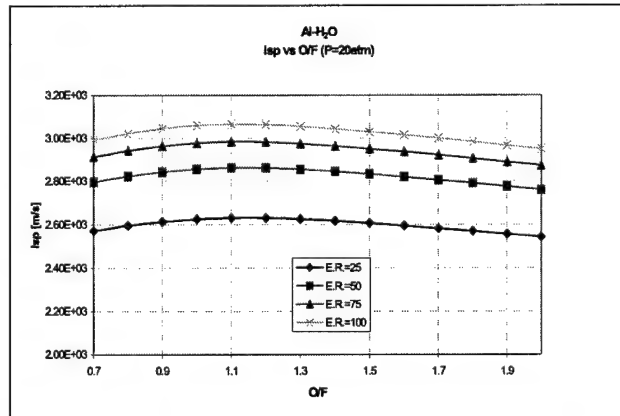


Figure 4: Isp vs O/F for Al-H<sub>2</sub>O system (P=20atm)

Assuming an inlet reactants temperature of about 300 K, the results indicate a Isp of order 3000 m/s over a wide range of pressures, oxidizer to fuel weight ratios (O/F) and pressure expansion ratios (E.R.).

The Isp dependence on pressure and O/F is mild; the main performance parameter is expansion ratio, leading to Isp variations of ~16% (see figures 1-5). Varying pressure and E.R., the maximum Isp always corresponds to O/F=1.1.

As predicted by reaction (2), Figure 6 shows the large concentration of H<sub>2</sub> and Al<sub>2</sub>O<sub>3</sub> at equilibrium. High equilibrium temperatures lead to hydrogen dissociation and high concentration of atomic H.

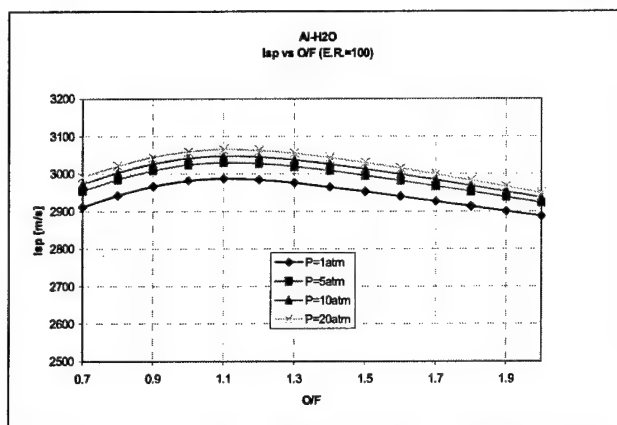


Figure 5: Isp vs O/F for Al-H<sub>2</sub>O system (E.R.=100)

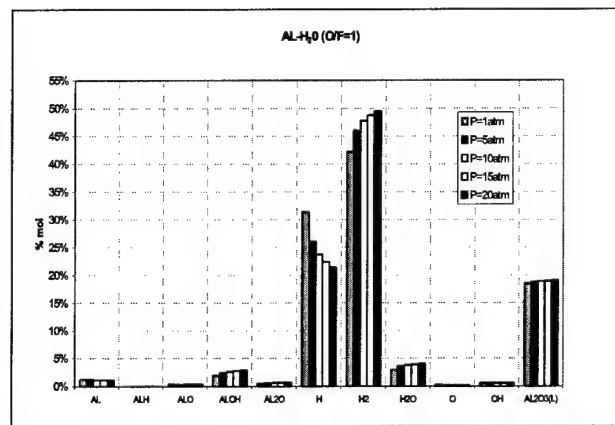


Figure 6: Species mole fractions(%) for Al-H<sub>2</sub>O system (O/F=1)

Figure 7 shows that *equilibrium* temperatures are of order 3500-4000 K, depending on pressure (see figure 7). These temperatures agree with those predicted by Von Grosse and Conway (see Ref. 46) about aluminum and oxygen combustion. They realized that the temperature of the flame around a metal burning particle with oxygen is characterize by a limit temperature equal to its oxide boiling temperature. The reason is that the difference between the heat released by combustion and that used to heat the mixture is lower than the heat needed to vaporize the oxide. The same happens with aluminum and water combustion. In fact, the heat released by the aluminum combustion with water  $2\text{Al}(\text{s}) + 3\text{H}_2\text{O}(\text{g}) \leftrightarrow \text{Al}_2\text{O}_3(\text{g}) + 3\text{H}_2$  is about 230 kcal/mol<sub>Al</sub> (where aluminum moles involving in the reaction are twice the Al<sub>2</sub>O<sub>3</sub> moles).

This heat issued by combustion is used as described below:

- ✓ an amount of about 38.3 kcal/mol<sub>Al<sub>2</sub>O<sub>3</sub></sub> (at P=1atm) is used to heat the *aluminum oxide* to its melting temperature;
- ✓ ~ 28.3 kcal/mol to melt *aluminum oxide*;
- ✓ ~ 17.9 kcal/mol to heat *alumina* to its boiling point.

If water is in the liquid phase at the combustor inlet, heat will be required also to vaporize water, in particular:

- ✓ about 0.557kcal/ mol<sub>H<sub>2</sub>O</sub> to heat *water* to its boiling point;
- ✓ and 1.438kcal/ mol<sub>H<sub>2</sub>O</sub> to boil *water*.

The difference between heat released by combustion and that necessary to heat and boil reactants is used to vaporize the oxide. Since the oxide vaporization heat (444 kcal/mol<sub>Al<sub>2</sub>O<sub>3</sub></sub>) is higher than this difference, the flame temperature will remain constant and equal to the boiling temperature. Thus the combustion temperature has an upper limit equal to the boiling temperature.

These high temperatures may pose severe material problems in practical operation, unless the equivalence ratio is reduced. In this case, the oxide addition lowers the adiabatic flame temperature both due to the effect on mixture Cp due to excess water and due to the heat absorbed by the endothermic reaction  $\text{H}_2 \rightarrow 2\text{H}$ . Even though lower temperatures could be favourable for materials, below the boiling temperature of aluminum, chemical reactions will occur on the aluminum surface,

and kinetics slowed down. Thus, in order to ensure that aluminum and water react in the gas phase, temperatures above the aluminum boiling temperature have to be supplied. Besides, decreasing temperature lowers Isp and density Isp. High temperatures may play a favourable role in maintaining a flame anchored in micropulsion chambers [Ref.47], where propellants with lower adiabatic flame temperature may be less stable due to their inherently larger heat losses.

Figures 8-10 show trends for a wide range of O/F at typical combustion chamber conditions for microrocket application ( $P=1$  atm, E.R=100).

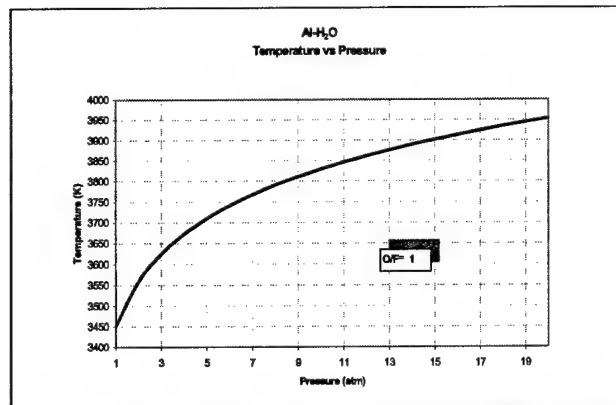


Figure 7: Temperature vs Pressure for Al-H<sub>2</sub>O system (O/F=1).

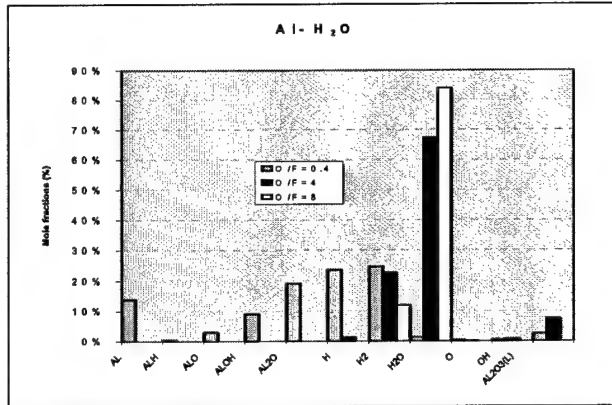


Figure 8 Species for Al-H<sub>2</sub>O system (P=1atm, E.R.=100).

Figure 9 requires a little explaining. At fixed pressure, temperature decreases as O/F ratio increases due to the increasing oxidizer concentration. Comparing fig. 8, fig. 9 and fig.10, the increasing O/F leads to the complete combustion of Aluminum and at the same time, to the formation of Al<sub>2</sub>O<sub>3</sub>(L). In all cases (O/F=0.4, 4, 8) the temperature is the result of competition between heat released by exothermic reactions forming Al<sub>2</sub>O<sub>3</sub>(L), and the heat absorbed by the endothermic reaction H<sub>2</sub> → 2H and by the presence of excess water.

For potential future applications, these figures show that assuming O/F=4.4 leads to Isp of about 2600 m/s (see fig.10) without requiring excessively high temperatures ( $\approx 2400$  K). However, at these temperature kinetics is slower due to surface reactions. Decreasing O/F to 3, a flame temperature (about 2800 K) higher than the aluminum boiling temperature is reached, speeding up chemical kinetics. At this temperature Isp is about 2750K.

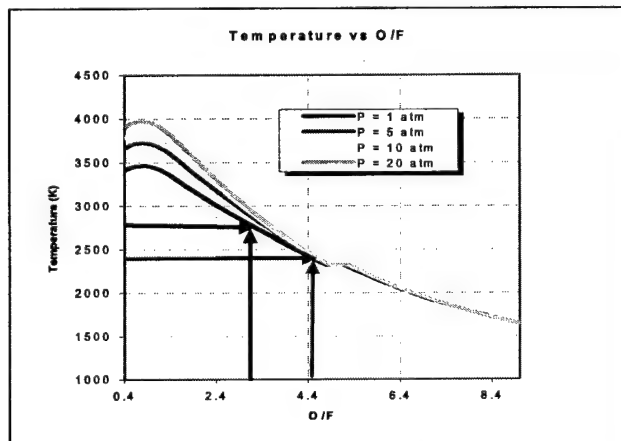


Figure 9 Temperature vs O/F for Al-H<sub>2</sub>O system (E.R.=100)

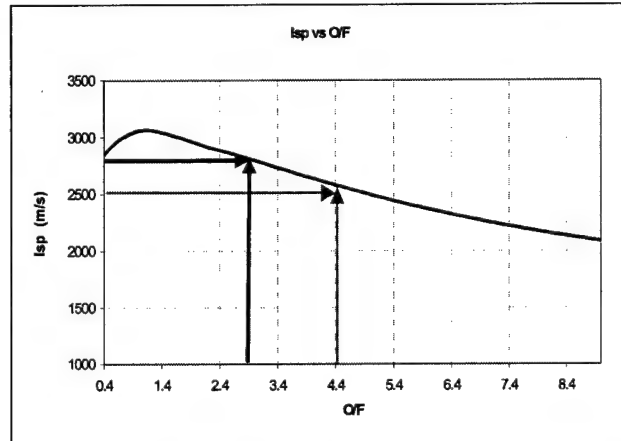


Figure 10: Isp vs O/F for Al-H<sub>2</sub>O system (P=1atm, E.R.=100)

Predicting the other extreme, i.e., "frozen" performance with the CEA600 code indicates a restricted range for O/F (5.2-7), outside which temperature is lower than the condensation temperature for  $\text{Al}_2\text{O}_3$  ( see Figures 11-12). Within this range, there are not substantial differences between the two cases (equilibrium and frozen).

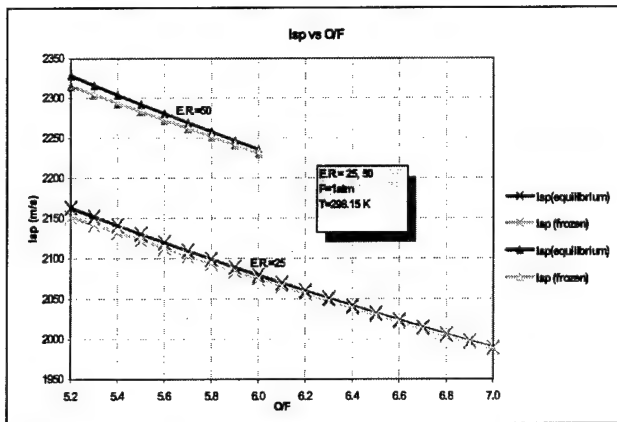


Figure 11 Isp vs O/F (Frozen and Equilibrium performance)

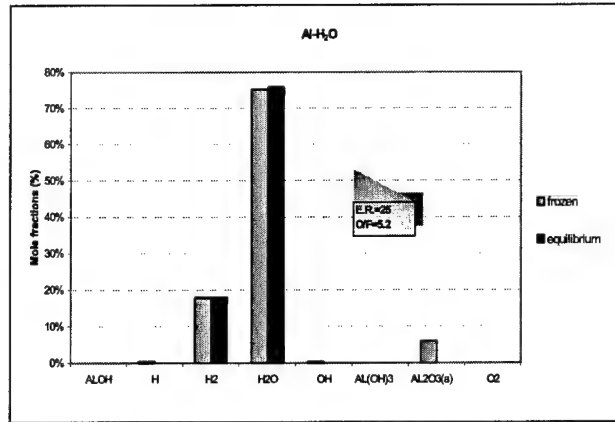


Figure 12 Species mole fractions (Frozen and Equilibrium performance)

As a point of interest, the effect of **hydrogen peroxide addition** to aluminum and water propellants was also analyzed.

Figure 13 shows that assuming 65%  $\text{H}_2\text{O}_2$  concentration in the oxidant solution (water/ hydrogen peroxide) increases the Isp over a broad range of O/F. This effect is negligible up to  $\text{O/F} \approx 1.1$ ; from this value on, the specific impulse grows from 2936 m/s to 3000 m/s (at  $P=10$  atm,  $\text{E.R.}=100$ ). For both mixture (Al/ $\text{H}_2\text{O}$  and Al/ $\text{H}_2\text{O}/\text{H}_2\text{O}_2$ (65%)), the thrust coefficient keeps constantly equal to 1.74 (for all O/F). Figure 14 shows species mole fractions at the combustor exit. It points out that even though hydrogen peroxide addition increases the overall molar weight (calculations indicate from 20.8 to 21.3), the specific impulse increases. This is due to the higher combustor temperature reached when burning aluminum with  $\text{H}_2\text{O}_2$  ( $T=3283.47$  K) rather than with pure  $\text{H}_2\text{O}$  ( $T=3140.46$  K).

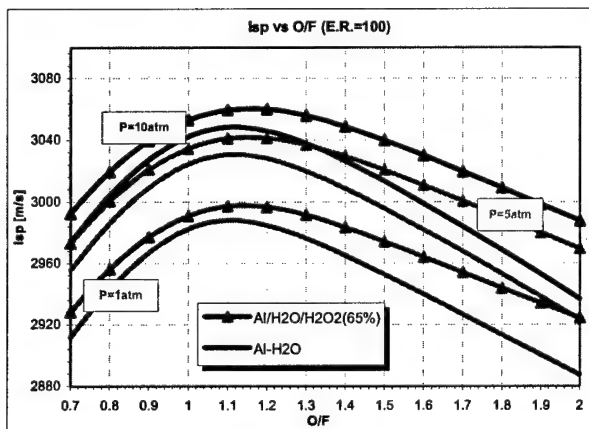


Figure 13 Isp trend with Al/H<sub>2</sub>O and Al/H<sub>2</sub>O/H<sub>2</sub>O<sub>2</sub>(65%)

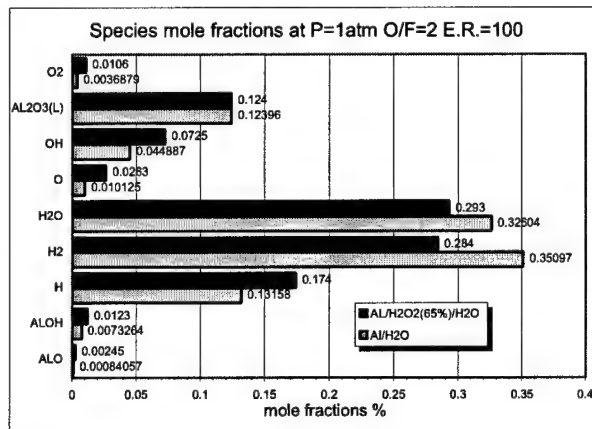


Figure 14 Species mole fractions (Equilibrium performance)

From a practical viewpoint, however, hydrogen peroxide addition would require a separate tank and pumping system, complicating the microrocket scheme. As compactness, simplicity and thrust are preferred to higher specific impulse, water as oxidizer looks a more interesting solution.

Figure below shows the comparison between the specific impulse obtained by aluminum/water combustion and by cracking product with oxygen at  $P=1$  atm,  $O/F=1$  and several area expansion ratio. Figure below points out a specific impulse increase by using aluminum instead of methanol of about 3%.

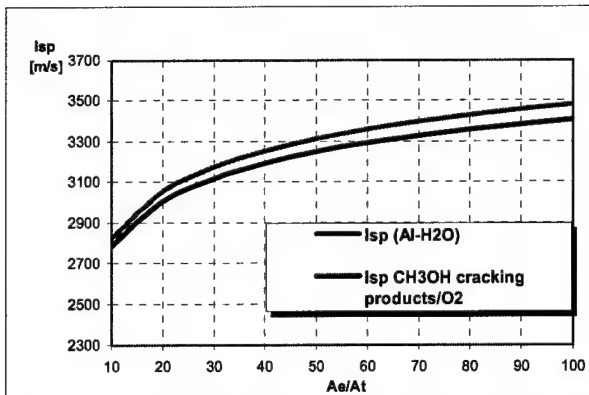


Figure 15 Isp vs Ae/At burning Al/H<sub>2</sub>O and methanol cracking products with oxygen

A further advantage, by using aluminum and water, is that storing water in the liquid phase is feasible even at atmospheric temperature and pressure, ensuring easier manufacturing pump and more compact design.

### 3 Burning aluminum particles with steam: Heating times

Since the Glassman criterion is critical to Al combustion, heating of particles is crucial. In this section, the heating and melting of a single particle of Al coated by a layer of Al<sub>2</sub>O<sub>3</sub> are analyzed. The calculations were performed assuming the hot gases temperature equal to alumina boiling temperature ~3272 K (corresponding to a stoichiometric mixture combustion temperature, see figure 10).

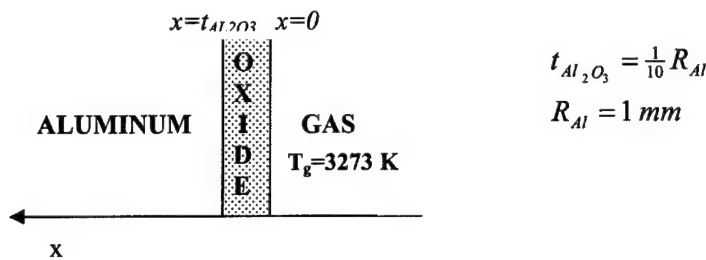
Melting and boiling temperatures and melting and boiling heats of aluminum and alumina are reported in the table below:

	Aluminum	Alumina
Melting temperature	933.52 K	2327 K
Boiling temperature	2792.15 K	3273 K
Melting heat	10.79 J/mol	118.407 kJ/mol
Boiling heat	293.4 kJ/mol	

Aluminum and alumina heating were calculated by writing two coupled energy equations (Ref. 46).

Since the oxide thickness ( $t_{Al2O3}$ ) is one tenth of the aluminum radius ( $R_{Al} \sim 1$  mm) we assumed a planar interface, and an one-dimensional analysis was performed. Thus, this analysis will be pessimistic with respect to the characteristic heating times.

We schematized the geometry as shown below:



In order to avoid adding momentum and mass equations, we assumed:

1. change of volume on solidification is neglected, so that the density is the same in both solid and liquid phases:  $\rho_l = \rho_s$
2. no fluid motion:  $v=0$

According to Fourier law, the energy equation in the solid phase is given for both Aluminum and alumina by:

$$\frac{\partial T_s}{\partial t} = \alpha_s \frac{\partial^2 T_s}{\partial x^2} \quad \text{where } \alpha_s = \frac{k_s}{\rho_s c_s} \quad (4)$$

The energy equation in liquid the phase is

$$\frac{\partial T_l}{\partial t} = \alpha_l \frac{\partial^2 T_l}{\partial x^2} \quad \text{where } \alpha_l = \frac{k_l}{\rho_l c_l} \quad (5)$$

where  $\alpha$ ,  $k$ ,  $\rho$  and  $c$  are respectively the diffusivity, the thermal conductivity, the density and the specific heat coefficients.

At the interface  $X(t)$  between the liquid and solid phase boundary conditions (6) and (7) have to be satisfied.

In particular, when  $x=X(t)$

$$T_s = T_l = T_m \quad (6)$$

The second boundary condition concerns the absorption of latent heat at this surface. In fact, the heat supplied by conduction is equal to the heat  $L\rho dX$  absorbed per unit area, making the separation surface move by a distance  $dX$ . This requires:

$$k_l \frac{\partial T_l}{\partial x} - k_s \frac{\partial T_s}{\partial x} = L\rho \frac{dX}{dt} \quad (7)$$

In order to solve the equations (4), (5), (6), (7), additional boundary conditions have to be furnished:

*Aluminum oxide B.C.:*

$$T_s = T_0 = 300 K \quad t = 0 \quad (8)$$

$$T_l = T_g = T_b = 3273 \text{ K} \quad x = 0 \quad (9)$$

where  $x=0$  corresponds to the separation surface between the oxide and the hot gases;

*Aluminum particle B.C.:*

$$T_s = T_0 = 300 \text{ K} \quad t = 0 \quad (10)$$

$$T_l = T_g = T_b = 3273 \text{ K} \quad x = 0 \quad (11)$$

where now  $x=0$  corresponds to the separation surface between the aluminum particle and its oxide.

This second B.C. condition supposes that the aluminum particles melting and heating occurs after the oxide reaches its boiling temperature. This assumption is again pessimistic, but lets quickly estimate a heating time.

The physical picture is as follows:

the  $\text{Al}_2\text{O}_3$  coating heats from 300 K to 2373 K: at this temperature the particle melts, and, once it is completely melted, temperature starts again to increase its up to the boiling point ( $\sim 3273$  K), above which temperature cannot increase. Thus, (following the assumption made) the aluminum particle begins to heat, its temperature increasing from 300 K to 933 K, followed by melting, heating of the melt to 2792 K, and then boiling. By looking at the equations above, the solution is:

$$T_s = T_0 + A \operatorname{erfc} \frac{x}{2\sqrt{\alpha_s t}} \quad (12)$$

$$T_l = T_g - B \operatorname{erf} \frac{x}{2\sqrt{\alpha_l t}} \quad (13)$$

where  $A$  and  $B$  are constants that must satisfy respectively (4), (8), and (5), (9).

Then (6) requires:

$$T_0 + A \operatorname{erfc} \frac{X}{2\sqrt{\alpha_s t}} = T_g - B \operatorname{erf} \frac{X}{2\sqrt{\alpha_l t}} = T_m \quad (14)$$

Since (14) has to be satisfied at all times,  $X$  must be proportional to  $t^{1/2}$ , i.e.,

$$X = 2\lambda \sqrt{\alpha_s t} \quad (15)$$

where  $\lambda$  is a numerical constant to be obtained from the condition (7).

Using (12), (13), (14) and (15), it follows:

$$\frac{e^{-\lambda^2}}{\operatorname{erfc} \lambda} - \frac{k_l}{k_s} \sqrt{\frac{\alpha_s}{\alpha_l}} \frac{(T_g - T_m)}{(T_m - T_0)} \frac{e^{-\frac{\alpha_s \lambda^2}{\alpha_l}}}{\operatorname{erf} \lambda \sqrt{\frac{\alpha_s}{\alpha_l}}} = \frac{\lambda L \sqrt{\pi}}{c_s (T_m - T_0)} \quad (16)$$

with  $T_s$  and  $T_l$  given respectively by:

$$T_s = T_0 + \frac{(T_m - T_0)}{\operatorname{erfc} \lambda} \operatorname{erfc} \frac{x}{2\sqrt{\alpha_s t}} \quad (17)$$

$$T_l = T_g - \frac{(T_g - T_m)}{\operatorname{erf}\left(\lambda \sqrt{\frac{\alpha_s}{\alpha_l}}\right)} \operatorname{erf} \frac{x}{2\sqrt{\alpha_l t}} \quad (18)$$

Equation (16) has been solved by the Newton Raphson method, and  $\lambda$  has been found to be  $\approx 1$ .  
Aluminum particle fusion has been studied in the same way.

Figure 16 shows the history of the surface of separation  $X$  between alumina solid and liquid phases. In particular, regions corresponding to radiiuses greater than  $X$  contain solid at temperatures  $T_s(r,t)$  dependent on time and radius, while, at radiiuses shorter than  $X$ , the region contains liquid at temperatures  $T_l(r,t)$ . This figure points out that the time required to melt *aluminum oxide*, the most important information needed, in fact, is about  $4.2 \mu s$  for  $t_{Al}=0.1 \text{ mm}$  ( $R_{Al}=1 \text{ mm}$ ). The  $\text{Al}_2\text{O}_3$  heat necessary to heat alumina up to its melting temperature is about  $1570.87 \text{ kJ/kg}$ , and the diffusive time is about:

$$t_{diff} = \frac{t_{Al2O3}^2}{\alpha_s} = 16.4 \mu s$$

that is of the same order of magnitude of the melting time. This was predictable, considering that melting heat is  $1116 \text{ kJ/kg}$ , i.e., slightly smaller (of about 0.7).

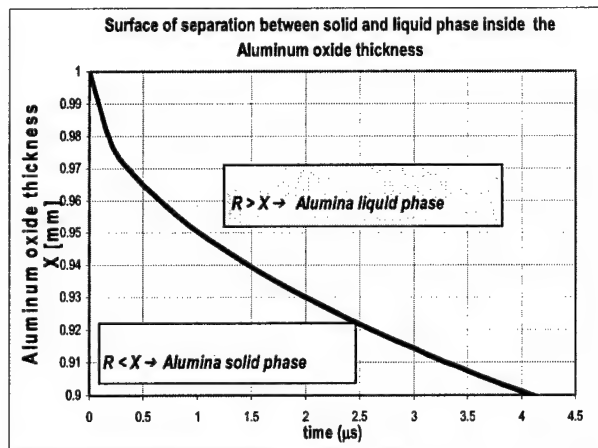


Figure 16 Alumina separation surface X history ( $R_{Al}=1 \text{ mm}$ )

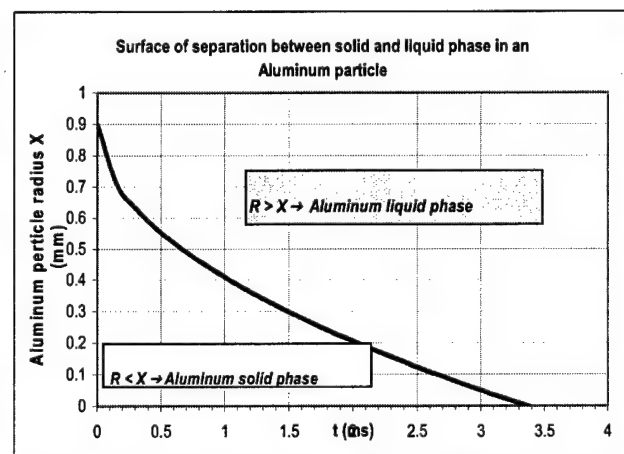


Figure 17 Aluminum separation surface X history ( $R_{Al}=1 \text{ mm}$ )

Figure 16 shows an *aluminum* melting time of about  $3.4 \text{ ms}$  (melting heat  $\approx 400 \text{ kJ/kg}$ ). The time needed to heat aluminum up to its melting temperature (melting heat is  $\sim 570 \text{ kJ/kg}$ ) is:

$$t_{diff} = \frac{R_{Al}^2}{\alpha_s} = 1.6 \text{ ms}.$$

These results point out that the whole process is controlled by aluminum heating, and the total time needed to heat and melt aluminum (given by the sum of all heats calculated before) is  $\sim 5 \text{ ms}$ .

The same analysis was performed assuming a radius of  $1E-7 \text{ m}$ .

Figure 18 shows alumina oxide heating times ( $4.2E-14$  s) are negligible compared to that of aluminum. In this case the time required for the aluminum particle to reach the melting temperature is of about  $1.1E-10$  s, and to be completely liquid  $4.2E-11$  s. Thus the total time needed to heat and melt aluminum ( $R_{Al}=1E-7$  m) is  $\sim 1.42E-10$  s.

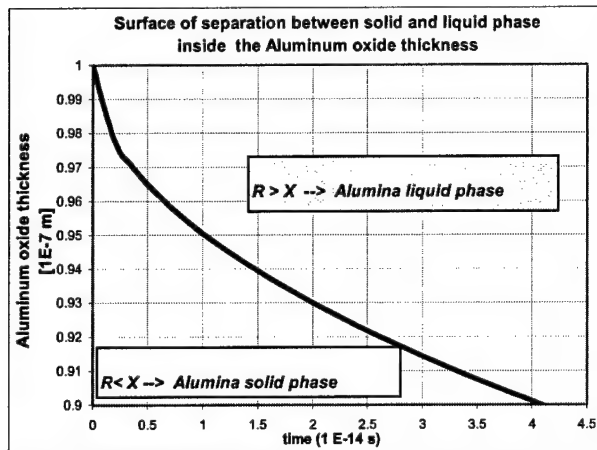


Figure 18 Alumina separation surface X history ( $R_{Al}=1E-7$  m)

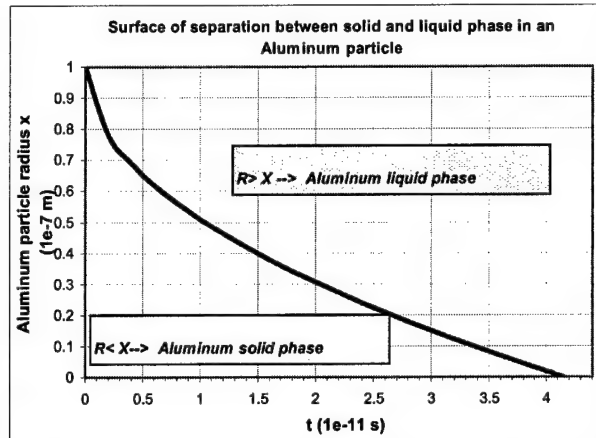


Figure 19 Aluminum separation surface X history ( $R_{Al}=1E-7$  m)

## 4 Kinetics and Ignition

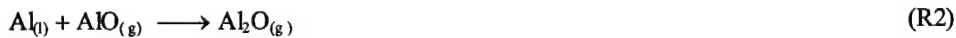
Because the theoretical performance of Al-H<sub>2</sub>O and its potentially short heating times look interesting, the next conceptual question is ignition and ignition delay, the latter controlling flame anchoring in a turbulent flame.

Detailed ignition of a single Al nanoparticle will be investigated in a separate study. Heating time of a nanoparticle inside the combustion products of Al-steam (about 3500K at O/F = 1) is of the order of  $5 \times 10^{-11}$  s. Melting time adds  $\sim 1E-10$  s.

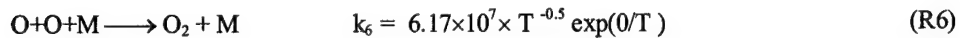
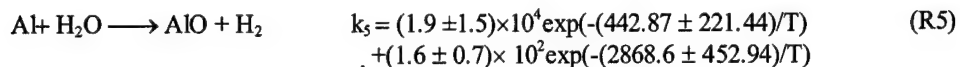
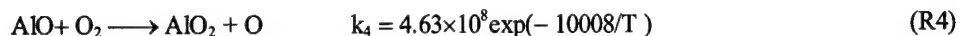
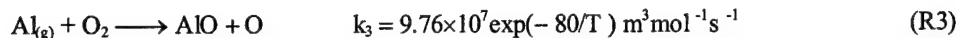
The time to ignite depends on Al-steam kinetics. Since Al ignition data are scarce, calculations were performed separating ignition reactions forming AlO and AlO<sub>2</sub> (mildly exothermic) and the condensation reactions, or completion reactions, forming Al<sub>2</sub>O<sub>3</sub>, that are much faster and more exothermic. In particular, for these preliminary calculations, gas phase reactions only were considered. Al-steam mixtures were assumed preheated at 2800K to analyze kinetic behavior at temperature higher than Al<sub>2</sub>O<sub>3</sub> boiling temperature (2700K). Simulations were performed using the kinetics rates k<sub>3</sub>, k<sub>4</sub>, k<sub>5</sub>, k<sub>6</sub> in [Ref.48, 49, 50].

The kinetics scheme is as follows:

Surface reactions:



Gas phase reactions:



Dissociation reaction:



Condensation:



The (R5) Arrhenius reaction rate points out that the Al and water combustion follows two reactions path. The first dominates at low temperatures, while the second dominates at high temperatures. As kinetic calculations are performed at high temperatures, only the second part was considered.

Figure 20, referring to an initial temperature of 2800K shows an interesting temperature history: after 1E-6s, this decreases to ~2660K (about 160K) because of endothermic formation of H atoms (see figure 21).

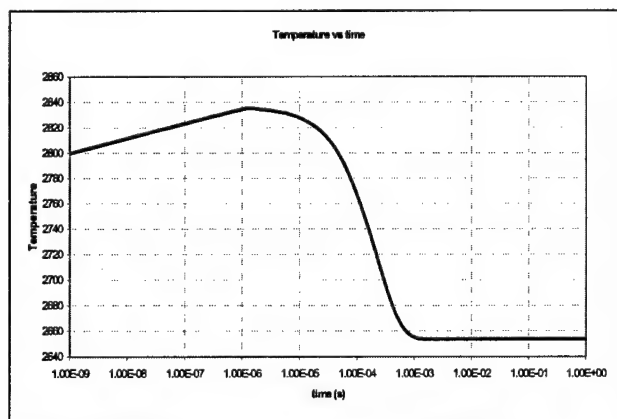


Figure 20: Temperature vs time for Al-H<sub>2</sub>O system  
(O/F=1, P=1atm); R3-R6 reactions only.

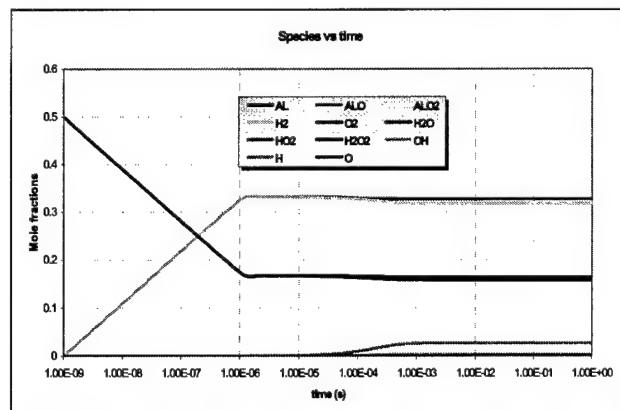


Figure 21: Species mole fractions for Al-H<sub>2</sub>O system  
(O/F=1, P=1atm).

It is important to underline that only mildly exothermic gas phase reactions were accounted for. Even so, these simulations predict ignition delays of order 10-5s at pressure 0.1MPa.

## 5 Impact on flame anchoring

In a turbulent flame kinetic times of order 0.1 ms or shorter are typically a sign of stable flame anchoring. For microrocket applications, however, this estimate must be consistent with physical size of the device: **this poses some challenges**. Assuming a scale of 1 cm for the chamber, at 2 MPa the Reynolds number could reach  $10^5$  to  $10^6$ , and the Kolmogorov scale would be then of order  $10^{-3}$  to  $10^{-4}$  cm. Turbulent (mixing) times ( $\sim k/\epsilon$ ) in this range of Reynolds numbers, using the Taylor scale for reference, are therefore of order  $10^{-4}$  to  $10^{-5}$  s. Although these are crude estimates, they point to a potential distributed combustion regime rather than to the more common ‘thin flame’, or flamelet regime. Distributed combustion may work efficiently, provided the reactants plus products be brought at sufficiently high temperature. Recycling wall heat losses to preheat water may obtain indeed this goal. In any event, from this preliminary analysis, Al-water combustion in microrockets should be investigated in greater depth.

## 6 Preliminary conclusions

In the first part of this paper, we briefly analyze the equilibrium performance (specific impulse, equilibrium temperature and composition in combustion chamber) of Aluminum using steam. To do this, we use the NASA CEA600 [4]. Performance with  $H_2O$  is interesting enough that it probably should be considered for satellite propulsion and perhaps for microrocket application(s).

Summarizing the results obtained, it is interesting to note that an high O/F ( $\sim 3$ ) leads to reasonably high temperature ( $\sim 2800$  K) and at the same time, high specific impulse ( $\sim 3000$  m/s). On the other side, these high temperatures are beneficial in maintaining a flame anchored in micropropulsion LRE chambers for satellites; at the same time the greater heat losses due to higher temperatures might be used to preheat and vaporize water before entering the microcombustion chamber. This scheme is more complex but is also more efficient.

Computations have shown that ALEX™ particles ensure heating times of a particle inside the combustion products of Al-steam of the order of  $5 \times 10^{-14}$  s and rapid melting ( $10^{-10}$  s) of its alumina layer with a total ignition delay time of about 1E-7 s. Under these conditions Al- $H_2O$  combustion looks promising for application to rocket engines for space applications in chemical microrocket. However, a major question is: how can the engine be started. Combustion of pure aluminum with water is a possible answer, burning pure Aluminum before its  $Al_2O_3$  coating formation.

## References

- [1] Janson, S.W., (1994), "Chemical and Electric Micropropulsion Concepts for Nanosatellites", AIAA paper 94-2998, presented at the AIAA Joint Propulsion Conference, Indianapolis, June 1994.
- [2] DeGroot, W.A., and Oleson, S.R., (1996), "Chemical Microthruster Options", AIAA Paper 96-2863, presented at the AIAA Joint Propulsion Conference, Buena Vista, FL, July 1996.
- [3] Mueller, J., (1997), "Thruster Options for Microspacecraft: A Review and Evaluation of Existing Hardware and Emerging Technologies", AIAA Paper 97-3058, presented at the AIAA Joint Propulsion Conference, Seattle, July 1997.
- [4] Noor, A.K., and Venneri, S. L., (1997), "Perspectives on Future Aeronautical and Space Systems", in: Future Aeronautical and Space Systems, ed. by A.K. Noor and S.L. Venneri, AIAA Progress in Astronautics and Aeronautics, Vol. 172, AIAA, Reston, VA, Chapter 1.
- [5] Hufenbach, B., and Saccoccia, G., editors, (1998), "Low Cost Spacecraft Propulsion Technologies for Small Satellites", Proc. of the ESA Workshop at ESA-ESTEC, Noordwijk, 19-20 March, 1998.
- [6] Dario, P., Carrozza, M.C., Fenu, A., and Mango, A., (1998), "Future Satellite Architecture with Emerging Technologies", ESA-ESTEC FUSARET Contract No. 12612 (ECT/97.185), Final Report, Noordwijk.
- [7] Shaw, G.B., Yashko, G., Schwartz, R., Wickert, D., and Hastings, D., (1999), "Analysis Tools and Architecture Issues for Distributed Satellite Systems", in: Microengineering Aerospace Systems, ed. by H. Helvajian, The Aerospace Press, El Segundo, CA, Ch. 15.
- [8] Mehrengany, M., and Roy, S., (1999), "Introduction to MEMS", in: Microengineering Aerospace Systems, ed. by H. Helvajian, The Aerospace Press, El Segundo, CA, p. 1.
- [9] Gad-el-haK, M., (2003), "Challenges in the Understanding of Microscale Phenomena", AIAA Paper 2003-439
- [10] Jaroff, L., (1996), "A New Lilliputian World of Micromachines", Time, Dec. 2, 1996, p. 66.
- [11] Janson, S.W., Helvajian, H., and Breuer, K., (1999), "Micropropulsion Systems for Aircraft and Spacecraft", in: Microengineering Aerospace Systems, ed. by H. Helvajian, The Aerospace Press, El Segundo, CA, Ch. 17.

- [12] Mueller, J., Chakraborty, I., Bame, D., Lawton, R., Forgrave, J., and Tang, W., (1998), "Micropropulsion Feasibility Studies at JPL", in: Proc. of the ESA Workshop at ESA-ESTEC, Noordwijk, 19-20 March, 1998.
- [13] Mueller, J., (1999), "A Review and Applicability Assessment of MEMS-based Microvalve Technologies for Microspacecraft propulsion", AIAA Paper 99-2725, presented at the 35th AIAA Joint propulsion Conference, 20-24 June 1999, LA.
- [14] Mueller, J., Vargo, S., Bame, D., Fitzgerald, D., and Tang, W., (1999), "Proof-of-Concept Demonstration of a micro-Isolation Valve", AIAA Paper 99-2726, presented at the 35th AIAA Joint propulsion Conference, 20-24 June 1999, LA.
- [15] Janson, S.W., Helvajian, H., Hansen, W.W., and Lodmell, J., (1999), "Batch-Fabricated CW Microthrusters for Kilogram-Class Spacecraft", AIAA Paper 99-2722, presented at the 35th AIAA Joint Propulsion Conference, 20-24 June 1999, LA.
- [16] Lawrence, T., (1998), "Research into Resistojet Rockets for Small Satellite Stationkeeping Applications", PhD Thesis, University of Surrey, UK, Chapter 5.
- [17] Rocket Research Corporation, (1976), "Development of Design and Scaling Criteria for Monopropellant Hydrazine Reactors Employing Shell 405 Spontaneous Catalyst", RRC Report RRC-66-R-76-Vol.II, Rocket Research Corporation, Seattle WA.
- [18] Alexeenko, A.A., Gimelshein, S.F., Levin, D.A., and Collins, R.J., (2000), "Numerical Modeling of Axisymmetric and Three-Dimensional Flows in MEMS nozzles", AIAA paper 2000-3668, presented at the 36th AIAA/ASME/SAE/ASEE Joint Propulsion Conference, July 16-19, 2000, Huntsville, Alabama.
- [19] Beardsley, T., (1999), "Fly me to the stars", Scientific American, Dec. 1999, p. 24.
- [20] Rodgers, S.L., Carrick, P.G., and Berman, M.R., (1999), "Propellants for Microthrusters", in: Microengineering Aerospace Systems, ed. by H. Helvajian, The Aerospace Press, El Segundo, CA, Ch. 16.
- [21] Ketsdever, A.D., and Mueller, J., (1999), "System Considerations and Design Options for Microspacecraft Propulsion Systems", AIAA Paper 99-2723, presented at the 35th AIAA Joint propulsion Conference, 20-24 June 1999, LA.
- [22] Ketsdever, A.D., Wadsworth, D.C., Wapner, P.G., Ivanov, M.S., and Markelov, G.N., (1999), "Fabrication and Predicted Performance of Conical DeLaval Micronozzles", AIAA Paper 99-2724, presented at the 35th AIAA Joint Propulsion Conference, 20-24 June 1999, LA.

- [23] Linan, A., and Williams, F.A., (1993), "Fundamental Aspects of Combustion", Oxford University Press, New York, pp.9-10 and Chapter 3.
- [24] Huzel, D.K., and Huang, D.H., (1992), "Modern Engineering for Design of Liquid-Propellant Rocket Engines", Prog. in Astron. And Aeron. Series, Vol. 147, AIAA, Washington, Section 4.4.
- [25] Filippi, M, and Bruno, C., (2000), "Reforming and Pyrolysis of Liquid Hydrocarbons and Partially Oxidized Fuels for Hypersonic Propulsion", Paper 5-ISICP-008-7-OP-CB, presented at the 5th ISICP, June 18-20, 2000, Stresa, Italy. Also published in: "Combustion of Energetic Materials", edited by K.K. Kuo and L. T. De Luca, Begell House, Inc., ISBN 1-56700-198-X, (2002).
- [26] Peters, N., (2000), "Turbulent Combustion", Cambridge University Press, p. 207 and 213.
- [27] Chomiak, J., (1990), "Combustion", Gordon and Breach, New York, Chapter 2, p. 55.
- [28] Gordon, S., McBride, B.J., "Computer Program for Calculation of Complex Chemical Equilibrium Compositions and Applications, Part II Users Manual and Program Description", NASA Ref. Pub. 1311, June 1996
- [29] Bruno C., Filippi M. and Czysz P. A., "Hydrocarbon Fuels Reforming for Hypersonic Propulsion", ISABE 99-7237, Florence, 5-10 September 1999
- [30] Yetter, R. A., Yang, V., Wang, Z., Wang, Y., "Development of Meso and Micro Scale Liquid Propellant Thrusters", AIAA Paper 2003-0676, presented at the 41th Aerospace Sciences Meeting & Exhibit, Reno, Nevada, 6-9 January 2003.
- [31] Ketsdever, A.D., and Mueller, J., "System Considerations and Design Options for Microspacecraft Propulsion Systems", AIAA Paper 99-2723, presented at the 35th AIAA Joint propulsion Conference, 20-24 June 1999, LA.
- [32] Ketsdever, A.D., Wadsworth, D.C., Wapner, P.G., Ivanov, M.S., and Markelov, G.N., (1999), "Fabrication and Predicted Performance of Conical DeLaval Micronozzles", AIAA Paper 99-2724, presented at the 35th AIAA Joint Propulsion Conference, 20-24 June 1999, LA.
- [33] Schneider, S., Boyarko, G., and Sun, C.-J., "Catalyzed Ignition of Bipropellants in Microtubes", AIAA Paper 2003-0674, presented at the 41st ASM, 6-9 January 2003, Reno, Nevada, 2003.
- [34] Margolis, S.B., and Gardner, T.J., "Extinction limits of nonadiabatic, catalyst-assisted flames in stagnation-point flow", Combust. Theory Modelling, Vol. 6, pp. 19-34, 2002.

- [35] Alexeenko, A.A., Levin, D.A., Fedosov, D.A., Gimelshein, S.F., and Collins, R.J., (2003), "Coupled Thermal and Fluid Analyses of Microthruster Flows", AIAA Paper 2003-0673.
- [36] Reed, B., (2003), "Decomposing Solid Micropropulsion Nozzle Performance Issue", AIAA Paper 2003-0672.
- [37] Ketsdever, A.D., (2003), "Microfluidics Research in MEMS Propulsion Systems", AIAA Paper 2003-0783.
- [38] Foote, J.P., Thompson, B.R., Lineberry, J.T., "Combustion of Aluminum with Steam for Underwater Propulsion", Advances in Chem. Propulsion, 2002, Ed. by G. Roy, ISBN 0-8493-1171-3.
- [39] Greiner, L., "Selection of High-Performance Propellants for Torpedoes", ARS J., Vol. 30, December: 1161-63.
- [40] Tepper, F., Kaledin, L., "Combustion Characteristics of Kerosene Containing ALEX NANO-ALUMINUM", presented at the 5th International Symposium on Special Topics in Chemical Propulsion: Combustion of Energetic Materials, Stresa, Italy, 18-22 June 2000.
- [41] Widener, J.F., Liang, Y., Beckstead, M.W., "Aluminum Combustion Modeling in Solid Propellant Environments", AIAA-99-0449.
- [42] Friedman, R., Macek, A., "Ignition on Combustion on Aluminum Particles in Hot Ambient Gasses", Combustion and Flames, Vol. 6, pp. 9-19, 1962.
- [43] Merzhanov, A.G., Grigorjev, Y.M. and Gal'chenko, Y.A., "Aluminum Ignition", Combustion and Flame, Vol. 29, 1977, pp. 1-14.
- [44] Kuehl, D.K., "Ignition on Combustion of Aluminum and Beryllium", AIAA J. 1965, Vol. 3, n. 12.
- [45] Gordon, S., McBride, B.J., "Computer Program for Calculation of Complex Chemical Equilibrium Compositions and Applications", Part II, Users Manual and Program Description, NASA Ref. 1311, June 1996.
- [46] Glassman, I., "Combustion", Academic Press, 1977.
- [47] Bruno, C., "Chemical Microthrusters: Effect of Scaling on Combustion", AIAA Paper 2001-3711, presented at the AIAA JPC, Salt Lake City, 8-11 July 2001.
- [48] Brooks, K.P., Beckstead, M.W., "Dynamics of Aluminum Combustion", Journal of Propulsion and Power, Vol. 11, n. 4, July-August 1995.

- [49] Liang, Y., Beckstead, M.W., Pudduppakkam, K.V., "Numerical Simulation of Unsteady, Single, Aluminum Particle Combustion", 36th JANNAF Combustion Meeting, CPIA n. 691, Vol. 1, 1999, p. 283-309.
- [50] Servaites, J., Krier, H., Melcher, J.C., and Burto, R.L., "Ignition and Combustion of Aluminum Particles in Shocked H<sub>2</sub>O/O<sub>2</sub>/Ar and CO<sub>2</sub>/O<sub>2</sub>/Ar Mixtures", Combustion and Flame, Vol. 125, p. 1040-1054, 2001.